Multiple mechanisms prevent ectopic condensation of FG nucleoporins in the cytoplasm

Laura Thomas[1], Peter Askjaer[2], and Geraldine Seydoux[1]

[1]HHMI and Department of Molecular Biology and Genetics, Johns Hopkins University School of Medicine, Baltimore, Maryland 21205

[2]Andalusian Center for Developmental Biology (CABD), CSIC/JA/Universidad Pablo de Olavide, Seville, Spain

Abstract

Nucleoporins (Nups) form the selective permeability barrier that separates the nucleoplasm from the cytoplasm. In addition to their localization at the nuclear envelope, Nups have been observed in cytoplasmic foci in many cell types. We have investigated the origin of Nup foci using *C. elegans* oocytes, which naturally accumulate high concentrations of Nups. We find that the foci derive from condensation of highly cohesive FG-Nups, which are maintained at concentrations right above the solubility limit in oocytes. Nup solubility is enhanced by chaperone activity and posttranslational modifications that also promote nuclear pore channel fluidity and pore disassembly during mitosis. Oocyte Nup foci dissolve during M phase and are not essential for embryonic viability. Overexpression of the highly cohesive FG-Nup, Nup98, in post-mitotic neurons leads to uncontrolled Nup aggregation and organismal paralysis, underscoring the importance of mechanisms that maintain Nup solubility in the cytoplasm.

Introduction

In all eukaryotes, the double-membraned nuclear envelope partitions the nucleoplasm from the cytoplasm and material is exchanged between the two compartments by way of nuclear pore complexes. Pore complexes are composed of at least 30 distinct nucleoporins (Nups) arranged in biochemically stable subcomplexes (Figure 1A) (Cohen-Fix and Askjaer, 2017; Hampoelz et al., 2019a). Approximately two-thirds of Nups are essential to scaffold and anchor pore complexes to the nuclear envelope. The remaining one-third contain large phenylalanine/glycine (FG) rich domains that are highly intrinsically disordered. FG-Nups are enriched in the central channel of the pore and readily from multivalent interactions both *in vivo* and *in vitro* (Frey et al., 2006; Labokha et al., 2012; Patel et al., 2007; Xu and Powers, 2013). Cohesive interactions among FG-Nups are critical for the formation of the permeability barrier and FG-Nup hydrogels recapitulate nuclear pore selectivity *in vitro* (Frey and Görlich, 2007; Hülsmann et al., 2012; Ng et al., 2021; Schmidt and Görlich, 2015; Strawn et al., 2004). This has led to the “selective phase” model in which the permeability barrier is established by interactions among FG-Nups that form a phase separated network (Ribbeck and Görlich, 2001; Schmidt and Görlich, 2016).

The intrinsic propensity of FG domains to form multivalent networks presents a potential danger if allowed to occur in an uncontrolled manner. Several mechanisms likely act to prevent aggregation of FG domains within the central channel of the pore. FG-Nups are extensively O-GlcNAcylated and this modification enhances Nup solubility *in vitro* (Labokha et al., 2012; Schmidt and Görlich, 2015) and has been proposed to relax FG domain interactions within the central channel (Ruba and Yang, 2016; Yoo and Mitchison, 2021). In the selective phase model, nuclear transport receptors (NTRs) cross the permeability barrier by binding and locally disrupting FG domain interactions (Schmidt and Görlich, 2016). NTRs have been reported to “chaperone” diverse aggregation-prone proteins including Nups (Guo et al., 2018; Harel et al., 2003; Hofweber et al., 2018; Hutten et al., 2020; Nachury et al., 2001; Padavannil et al., 2019; Walther et al., 2003), raising the possibility that NTR binding enhances FG-Nup solubility. Finally, phosphorylation plays a major role in pore complex disassembly during M phase (Kutay et al., 2021), implicating this modification in preventing interactions among Nups.

In addition to their localization at the nuclear envelope, Nups have been observed in discrete cytoplasmic foci in virtually all cell types (Cordes et al., 1996; Raghunayakula et al., 2015; Ren et al., 2019). Based on early electron microscopy studies these structures were proposed to represent annulate lamellae, a specialized subdomain of the endoplasmic reticulum rich in pore complexes (Kessel, 1989). Prior studies have proposed that annulate lamellae may act as stores of ready-made pore complexes to supplement the nuclear envelope during rapid cell divisions (Hampoelz et al., 2016; Ren et al., 2019), though the exact function of these structures remains unclear (Stafstrom and Staehelin, 1984). Cytoplasmic Nup foci have additionally been proposed to correspond to structures distinct from annulate lamellae that function in nuclear pore inheritance (Colombi et al., 2013) or pore biogenesis in the cytoplasm (Hampoelz et al., 2019b). Nups are also frequently enriched in pathological cytoplasmic inclusions that are hallmarks of neurodegenerative disease (Chandra and Lusk, 2022; Fallini et al., 2020; Hutten and Dormann, 2020), leading to the proposal that Nups become sequestered and depleted from nuclear pores under disease conditions (Gasset-Rosa et al., 2019; Zhang et al., 2018). Condensation of FG-Nup fusion oncogenes contributes to certain cancers (Chandra et al., 2022; Terlecki-Zaniewicz et al., 2021; Zhou and Yang, 2014), and recent studies have found that cytoplasmic FG-Nups drive aggregation of TDP-43 in ALS/FTLD and following traumatic brain injury (Anderson et al., 2021; Gleixner et al., 2022). Together, these observations raise the possibility that ectopic condensation of FG-Nups may drive protein aggregation and disease progression.

Here we use *C. elegans* oocytes, which have abundant, endogenous Nup foci (Patterson et al., 2011; Pitt et al., 2000; Sheth et al., 2010), as a model to investigate the function of Nup structures in the cytoplasm. We find that cytoplasmic Nup foci contain only a subset of Nups and do not always colocalize with membranes, indicating that these structures do not represent pore complexes. Instead, we propose that, as in the central channel of nuclear pores, cohesive interactions among FG domains drive condensation of Nups in the cytoplasm. We find that the solubility of cytoplasmic Nups is controlled by the same mechanisms that regulate network formation in the central channel, including posttranslational modifications and NTR binding. Finally, in contrast to prior models proposing that Nup foci function in different aspects of pore biogenesis, we find that these structures are transient and do not serve an essential biological role.

Instead, our data suggest that uncontrolled Nup condensation presents a potential danger that must be counteracted by energy-consuming mechanisms.

Results

Cytoplasm-facing Nups form cytoplasmic foci in *C. elegans* oocytes

To systematically characterize Nup distribution in oocytes, we used a collection of genomically-encoded tags, transgenes, and antibodies against 16 Nups (including one or more representatives of each subcomplex) and the Nup358 binding partners RanGAP and NXF1 (Figure 1A; Table S1). In *C. elegans* hermaphrodites, oocytes are arranged in the oviduct in order of maturation with the oldest oocyte (-1 position) nearest the spermatheca. The -1 oocyte is activated by a secreted sperm signal to undergo nuclear envelope breakdown (NEBD) in preparation for meiotic divisions, ovulation, and fertilization (Figure 1B) (Huelgas-Morales and Greenstein, 2018). We focused our initial survey on oocytes in the -4 and -3 positions of day 2 adult hermaphrodites where Nup foci are most prominent.

As expected, all Nups tested localized to the nuclear envelope (Figures 1C and S1A). Nuclear basket and Y complex Nups additionally localized to the nucleoplasm and meiotic chromosomes, respectively, as previously described (Hamed et al., 2021; Hattersley et al., 2016; Wu et al., 2001). A subset of Nups also localized to cytoplasmic foci, including FG-Nups of the central channel and cytoplasmic filaments (Nup62, Nup98, Nup214, and Nup358) and their binding partners (Y complex Nups, Nup88, RanGAP, and NXF1) (Figures 1C, S1A, and S1B). The transmembrane Nups gp210 and NCD1 could be detected throughout the endoplasmic reticulum as previously described (Galy et al., 2008), but did not enrich in cytoplasmic foci, nor did Nup35, an inner ring complex Nup. We also analyzed the distribution of a subset of Nups in 4-cell stage embryos and obtained the same results except for Nup35, which did not form foci in oocytes but did in embryos (Figures S1C and D). We conclude that cytoplasmic Nup foci primarily enrich cytoplasm-facing FG-Nups and their binding partners (Figure 1A).

Co-staining experiments using the mAb414 antibody (Davis and Blobel, 1986), which recognizes multiple Nups, suggested that distinct Nups co-localize in the same foci (Figures S1A and D). To examine this systematically, we crossed a subset of GFP-tagged Nups pairwise with Nup62::wrmScarlet. As expected all Nups tested colocalized with Nup62::wrmScarlet at the nuclear envelope (Figure 1D). Nups that localize to cytoplasmic foci (Nup85, Nup88, Nup98, and Nup358) additionally colocalized with Nup62::wrmScarlet in all foci, confirming that the foci are assemblies of multiple Nups. Additionally, quantification of the ratio of the GFP-tagged Nup to Nup62::wrmScarlet revealed that each Nup accumulates in fixed stoichiometry relative to Nup62 at the nuclear envelope, but with variable stoichiometry in the cytoplasmic foci (Figure 1D).

A recent study reported that cytoplasmic Nup foci do not overlap with endoplasmic reticulum membranes in HeLa or Cos7 cells (Ren et al., 2019). To determine whether Nup foci in *C. elegans* colocalize with membranes, we visualized GFP::Nup88 in the presence of a luminal marker of the endoplasmic reticulum and nuclear envelope (Fan et al., 2020). As expected, GFP::Nup88 at the nuclear envelope colocalized with the reporter, but only a subset (20%) of GFP::Nup88 cytoplasmic foci overlapped with the endoplasmic reticulum (Figure 1E), indicating that the majority of cytoplasmic Nup foci in oocytes are not transmembrane structures.

In summary, our observations indicate that cytoplasmic Nup foci specifically accumulate cytoplasm-facing FG-Nups and their binding partners in varying stochiometric amounts, lack critical nuclear pore scaffolds including transmembrane and inner ring complex Nups, and do not always associate with membranes. These observations suggest that Nup foci are unlikely to assemble by the same mechanisms that yield mature nuclear pores and may form instead by spontaneous condensation of FG-Nups.

Nup foci assembly is driven by FG-Nups that accumulate in excess of C_{sat} in oocytes

Condensation is sensitive to concentration: proteins de-mix into dense and dilute phases when concentration exceeds the saturation concentration (C_{sat}), the maximum concentration allowed in the soluble, dilute phase (Alberti et al., 2019). Proteins maintained at concentrations just above C_{sat} will form condensates, but these will account for only a small proportion of total molecules, most of which will remain in the soluble, dilute phase. To determine the amount of Nup molecules in foci, we used Imaris software to quantify the relative amount of Nup fluorescence in nuclei, the cytoplasm, and cytoplasmic foci as a percent of total fluorescence in oocytes (see materials and methods). This analysis revealed that, in day 2 adults, only a minority (<3%) of Nup molecules accumulate in cytoplasmic foci (Figure 2A). The majority distribute between a nuclear pool (~30-40%) and a diffuse cytoplasmic pool (~60-70%). The cytoplasmic pool is the least concentrated but largest by volume and is readily visualized in sum projection photomicrographs (Figure S2A). We also found that Nup foci are highly influenced by animal age and increase significantly between days 1 and 2 of adulthood (Figure S2B), therefore, animals were carefully age-matched in all experiments.

The observation that cytoplasmic Nup foci represent only a minor fraction suggests that the concentration of FG-Nups in oocytes is near C_{sat} and that depletion of a single FG-Nup may be sufficient to lower FG-Nup concentration below C_{sat} and eliminate Nup foci. Consistent with this prediction, we found that RNAi depletion of the cytoplasm-facing “scaffold” FG-Nups (Nup62, Nup98, Nup214, or Nup358) and the FG-Nup binding partner Nup88, strongly reduced the proportion of GFP::Nup85 in Nup foci (Figures 2B, S2C-E), without affecting GFP::Nup85 levels at the nuclear envelope (Figure 2B). In contrast, depletion of non-FG or nucleoplasmic Nups had no effect, whereas loss of Nup35 or the transmembrane Nups NDC1 or gp210 enhanced the formation of Nup foci, including inducing formation of ectopic Nup foci in the distal germline (Figures 2B, 2C, S2C, and S2F). Nup35 and NDC1 are structural Nups required for pore assembly (Mansfeld et al., 2006; Mauro et al., 2022; Ródenas et al., 2009) and, as expected, depletion of these Nups also decreased the intensity of Nups at the nuclear envelope. Together these findings suggest that high concentrations of the FG-Nups Nup62, Nup98, Nup214, and Nup358 in the cytoplasm drive Nup foci assembly. Depletion of Nup88, which is structured but interacts with multiple subcomplexes containing FG-Nups (Fornerod et al., 1997; Griffis et al., 2003;

Xylourgidis et al., 2006; Yoshida et al., 2011), partially depleted Nup foci, suggesting that interactions between FG-Nups subcomplexes contribute to foci formation.

To directly test whether increased levels of FG-Nups cause foci formation, we generated a transgenic strain with an extra copy of *nup214::wrmScarlet* expressed under the control of the germline-specific *mex-5* promoter (Fan et al., 2020). We found that overexpression of Nup214::wrmScarlet was sufficient to increase the proportion of endogenous mNeonGreen::Nup358 in Nup foci by 4-fold (Figures 3A and S3A). Prior RNAi experiments indicate that Nup214 is non-essential in *C. elegans* (Galy et al., 2003), therefore we used CRISPR genome engineering to generate a complete deletion of the *nup214* locus and examined *nup214*Δ homozygous mutants for Nup foci. Using three independent markers (mNeonGreen::Nup358, RanGAP::wrmScarlet, and mAb414), we found that Nup foci were significantly reduced in *nup214*Δ mutant oocytes and embryos (Figures 3B, 3C, and S3B). Nup foci were also largely absent in a second independently obtained *nup214* deletion allele (Figure S3C). Despite lacking robust Nup foci, *nup214*Δ embryos were 100% viable (Figure 3D).

Nup214 is required for Nup88 stabilization and targeting to pore complexes (Xylourgidis et al., 2006), and consistent with lack of Nup214 activity, GFP::Nup88 was largely mislocalized to the cytoplasm in *nup214*Δ mutants (Figure S3D). This observation further suggests that specific Nups drive foci formation, as *nup214*Δ mutants lack robust foci despite mislocalization of Nup88 to the cytoplasm. We conclude that Nup foci result primarily from condensation of FG-Nups, which are maintained at concentrations just above solubility in oocytes.

Nup solubility is responsive to cell cycle phase

Although Nup foci are readily apparent in growing oocytes (-3 and -4 positions in the oviduct), they are largely absent from maturing oocytes (-1 position) which undergo NEBD in preparation for the meiotic divisions (Figures 1B and 4A). To distinguish whether this difference is due to a change in Nup concentration or solubility, we compared the cytoplasmic concentration of the FG scaffold mNeonGreen::Nup358 across -3 to -1 oocytes. We found that the cytoplasmic concentration and total levels of mNeonGreen::Nup358 increase from the -3 to the -1 oocyte (Figures 4A and S4A). In the same period, the percent of mNeonGreen::Nup358 in cytoplasmic foci decreased, most dramatically between the -3 and -2 oocyte, with no detectable foci remaining in most -1 oocytes (Figure 4A). In early embryos, Nup foci cycled with each cell division, disassembling at NEBD during mitosis and reassembling in interphase (Figure 4B). The cytoplasmic Nup concentration increased at each mitosis, while total Nup levels remained stable (Figure 4B and S4B).

These observations suggest that entry into M phase increases the solubility of Nups, both in cytoplasmic foci as well as at the nuclear envelope. Consistent with this hypothesis, we found that GFP::Nup88 remained in foci in the -1 oocytes of *fog-2(q71)* females, which do not initiate M phase and do not disassemble nuclear pores (Figure 4C) (Schedl and Kimble, 1988). Unlike wild-type oocytes which are continuously ovulated, *fog-2(q71)* oocytes remain in the oviduct and accumulate ~50% more total GFP::Nup88 and ~14-fold more GFP::Nup88 in foci compared to wild-type (Figures 4C and S4C). Arrested oocytes also accumulated Nup35 and ELYS in foci, which were not observed in foci in growing oocytes (Figure S4D). *fog-2(q71)* arrested oocytes, however, did not condense the stress granule scaffold G3BP, despite increased levels of G3BP (Figures 4C and S4E). We conclude that the solubility of Nups in the cytoplasm is highly tuned to cell cycle stage and may be subject to the same regulatory processes that drive nuclear pore dissolution during M phase.

Phosphorylation, GlcNAcylation, and the nuclear transport receptor CRM1 promote Nup solubility

Nuclear pore disassembly during NEBD is well characterized and driven in large part by Nup phosphorylation (Kutay et al., 2021). To test whether cell cycle kinases similarly regulate the solubility of cytoplasmic Nups, we used RNAi to deplete PLK1 and CDK1, two kinases that phosphorylate Nups to drive nuclear pore disassembly and are active during oocyte maturation in *C. elegans* (Chase et al., 2000; De Souza et al., 2004; Huelgas-Morales and Greenstein, 2018; Laurell et al., 2011; Linder et al., 2017; Martino et al., 2017; Onischenko et al., 2005; Rahman et al., 2015). Additionally, the CDK1 binding partner cyclin B has been observed to localize to cytoplasmic Nup structures in *Xenopus* oocytes (Beckhelling et al., 2003). In agreement with this study, we observed that CDK1 enriches in Nup foci in *C. elegans* oocytes (Figure S5A). We found that RNAi depletion of both PLK1 and CDK1 increased the percent of Nup88 in foci as well as at the nuclear envelope (Figures 5A, 5B, S5B, and S5C). Inhibition of the phosphatase PP2A was reported to block nuclear pore complex and Nup foci assembly in *Drosophila* embryos (Onischenko et al., 2005). Similarly, we found that RNAi depletion of the scaffolding subunit of PP2A led to a striking loss of Nup foci as well as depletion of Nup88 from the nuclear envelope (Figures 5A, 5B, S5B, and S5C). We conclude that Nup phosphorylation by cell cycle kinases increases Nup solubility in oocytes and that PP2A phosphatase activity counteracts this effect.

FG-Nups are also heavily modified by O-GlcNAcylation, which has been previously proposed to limit FG domain interactions in the central channel (Ruba and Yang, 2016; Yoo and Mitchison, 2021). The anti-GlcNAc RL2 antibody stained the nuclear envelope and Nup foci in oocytes as well as embryos (Figures S5D and E). O-GlcNAcylation is catalyzed by the enzyme O-GlcNAc transferase (OGT), and endogenously-tagged OGT::GFP was enriched in Nup foci (Figure S5F). *ogt*Δ mutant animals lacked Nup O-GlcNAcylation as previously described (Figures S5D and E) (Hanover et al., 2005) and exhibited enhanced formation of Nup foci (Figures 5A, 5C, S5B, and S5G). We also visualized Nup foci in a loss of function allele of the *C. elegans* O-GlcNAcase (OGA) reported to exhibit higher levels of Nup GlcNAcylation in embryos (Forsythe et al., 2006). We did not detect a significant change in Nup foci in the *oga* mutant, suggesting that, in oocytes, Nups may be sufficiently O-GlcNAcylated such that loss of OGA activity does not affect Nup solubility.

Recent studies have suggested that nuclear transport receptors (NTRs) function as chaperones to prevent aggregation of intrinsically disordered proteins (Guo et al., 2018; Hofweber et al., 2018; Hutten et al., 2020). The exportin CRM1 makes high affinity interactions with the FG-Nup scaffolds Nup214 and Nup358 (Port et al., 2015; Ritterhoff et al., 2016; Tan et al., 2018). We found that endogenously tagged CRM1::mNeonGreen, as well as the NTR transportin::mNeonGreen, distribute between the cytoplasm (~75%) and nucleoplasm (~25%), with a minor fraction (<1%) present at cytoplasmic Nup foci (Figures S6A and B). RNAi depletion of CRM1 led to an increase in Nup foci formation (Figures 5A, 5D, S5B, S6C, and S6D). This effect is unlikely to be due to impaired nuclear export, as Nup foci were not altered in worms treated for 4 hours with the CRM1 inhibitor leptomycin B (LMB), which binds within the NES binding groove to prevent interaction with NES cargos (Figures 5A, 5D, S5B, S6D, and S6E) (Sun et al., 2013). RNAi depletion of transportin did not affect Nup solubility (Figures S6F and G), indicating that CRM1 may be uniquely effective at solubilizing cytoplasmic Nups in oocytes. In summary, we conclude that Nup solubility is enhanced by phosphorylation, O-GlcNAcylation, and CRM1 binding.

Nup98 overexpression in neurons leads to ectopic Nup foci, Nup depletion from the nuclear envelope, and neuronal dysfunction

Outside of oocytes, we rarely observed cytoplasmic Nup foci in wild-type hermaphrodites. The concentration of Nup358 in terminally differentiated intestinal cells was ~30% that of oocytes (Figure 6A), suggesting that somatic cells maintain FG-Nup concentration well below C_{sat}. We therefore wondered whether overexpression of an FG-Nup might be sufficient to drive the formation of FG-Nup foci in somatic cells. Nup98 is unique among Nups as being highly cohesive and interacting with multiple structured Nups (Onischenko et al., 2017; Schmidt and Görlich, 2016). Overexpression of Nup98 from a transgene driven by the neuron-specific *rab-3* promoter led to abundant cytoplasmic foci, that were not observed when Nup98 is only expressed from its endogenous locus (Figure S7A). Interestingly, the *rab-3p*::Nup98 animals had shorter lifespans (Figure S7B) and appeared uncoordinated (barely moving) on plates or in liquid (Figure 6B and Videos S1 and 2), consistent with neuronal dysfunction and paralysis (Dimitriadi and Hart, 2010).

To determine whether Nup98 condensates disrupts nuclear pore assembly, we examined the expression of an endogenous Nup (Nup62) in the presence of the *rab-3p*::Nup98 transgene. In non-neuronal cells that did not express the transgene, Nup62::wrmScarlet localized to the nuclear envelope as in wild-type (Figures 6C and D). In contrast, in neurons overexpressing Nup98, Nup62::wrmScarlet was recruited to the cytoplasmic Nup98 foci and depleted from the nuclear envelope (Figure 6D). Interestingly, neuronal overexpression of another FG-Nup, Nup358, led to cytoplasmic foci that did not recruit an endogenous Nup and did not cause paralysis, though swimming behavior was slightly altered (Figures 6E, S7C, and S7D and Videos S3 and 4). We conclude that, in somatic cells, some cytoplasmic Nup foci are tolerated, while others containing the highly cohesive Nup98 interfere with nuclear pore assembly and cause cellular disfunction.

Discussion

In this study, we have characterized the Nup condensates that form in the cytoplasm of *C. elegans* oocytes and early embryos. Our findings (summarized in Figure 7) indicate that, as cytoplasmic Nup levels rise in growing oocytes, cohesive interactions among Nup FG domains drive Nup condensation in the cytoplasm. Although Nup condensates appear prominent when observed by fluorescent microscopy, they account for less than 3% of total cellular Nup, as phosphorylation, GlcNAcylation, and CRM1 chaperoning maintain the majority of Nup molecules in a soluble state. Oocyte Nup condensates disassemble during M phase and are not required for embryonic viability. Ectopic assembly of Nup condensates in post-mitotic neurons, however, can deplete Nups from the nuclear envelope and cause organismal paralysis. We conclude that cytoplasmic Nup condensates do not serve an essential function and are potentially toxic compartments.

Cytoplasmic Nup foci arise by condensation of FG-Nups and their binding partners

Several lines of evidence indicate that Nup foci in *C. elegans* oocytes and embryos are condensates that arise when FG-Nups exceed their solubility limit. First, Nup foci only contain cytoplasm-facing FG-Nups and their binding partners and lack nucleoporins essential for pore assembly including transmembrane Nups. Second, unlike nuclear pores, Nup foci display heterogeneous Nup stoichiometry and the majority do not colocalize with membranes. Third, Nup foci account for less than 3% of total Nup molecules and depletion and overexpression of FG-Nups eliminate and enhance, respectively, foci formation, consistent with a concentration-dependent process. Depletion of Nup88, which is structured but associates with multiple FG-Nups, partially reduced foci formation, whereas depletion of the central channel FG-Nup Nup54 had no significant effect. Together, this suggests that interactions among specific FG-Nups, including Nup62, Nup98, Nup214, and Nup358, and their binding partner Nup88 scaffold cytoplasmic condensates.

Our observations do not support the view that Nup foci correspond to annulate lamellae or another type of nuclear pore precursor, which would be expected to mirror nuclear pore stoichiometry and membrane association. Electron microscopy studies reported that annulate lamellae were absent in growing oocytes and embryos and present in only ~10% of arrested oocytes in *C. elegans* (Langerak et al., 2019; Patterson et al., 2011; Pitt et al., 2000). In contrast, we observe Nup foci in 100% of growing or arrested oocytes as well as embryos. While the transmembrane Nups NDC1 and gp210 were not enriched in foci in oocytes, a recent study found that a subset of Nup160::GFP foci overlapped with NDC1 in *C. elegans* 1-cell embryos (Mauro et al., 2022). We cannot exclude the possibility that a small subset of Nup foci correspond to annulate lamellae, however, we favor the view that the majority are “accidental” condensates that form when Nup levels exceed the solubility threshold.

Cytoplasmic Nup foci have been observed by fluorescent microscopy across diverse cell types ranging from primary neurons to transformed cell lines (Cordes et al., 1996; Raghunayakula et al., 2015). Consistent with our findings, recent systematic tagging of endogenous Nups in HEK293T cells revealed that cytoplasm-facing FG-Nups and their binding partners accumulate in cytoplasmic foci, but Nup153, which faces the nucleoplasm, does not (Cho et al., 2022). Similarly, Colombi et al., 2013 reported that Nup foci exist in yeast that contain multiple FG-Nups but lack transmembrane or inner ring complex Nups, and suggested that the foci did not represent annulate lamellae. We also found that the FG-Nup Nup214 forms numerous foci in yeast cells, but nucleoplasm-facing Nup50 and Nup153 do not (Figure S7E). Together these observations suggest that most Nup foci do not represent fully formed pores, as expected for annulate lamellae. We suggest instead that Nup foci arise in cells whenever the concentration of FG-Nups in the cytoplasm exceeds the solubility threshold. Consistent with this view, depletion of scaffold nucleoporins that liberate FG-

Nups enhance foci formation in *C. elegans* oocytes (Figures 2 and S2), yeast (Makio et al., 2009) and HeLa cells (Raghunayakula et al., 2015).

Phosphorylation, GlcNAcylation, and CRM1-mediated chaperoning limit Nup condensation

Our findings suggest that the same mechanisms that regulate Nups at nuclear pores regulate Nup solubility in the cytoplasm. Phosphorylation by the mitotic kinases PLK1 and CDK1 drive pore complex disassembly during M phase (Kutay et al., 2021) and we find that the same kinases promote Nup solubility in oocytes. Given the high number of annotated phosphorylation sites for most Nups (Hampoelz et al., 2019a), it is likely that multiple kinases act combinatorially to promote Nup solubility, including NIMA and DYRK kinases which have been implicated in nuclear pore disassembly (De Souza et al., 2004; Laurell et al., 2011; Wippich et al., 2013). Consistent with phosphorylation driving Nup solubility, cellular fractionation experiments found that Nups in the cytoplasm are phosphorylated (Onischenko et al., 2004). Our observations indicate that GlcNAcylation additionally contributes to Nup solubility in the cytoplasm, a modification that has also been proposed to prevent non-productive interactions within the nuclear pore central channel (Ruba and Yang, 2016; Yoo and Mitchison, 2021). Numerous studies have reported a protective role for O-GlcNAcylation in neurodegenerative disease (Lee et al., 2021), raising the possibility that this modification plays a general solubilizing role for aggregation-prone proteins.

We find that Nup solubility is also enhanced by the NTR CRM1. NTRs cross the permeability barrier through direct, transient association with Nup FG domains (Bayliss et al. 1999; Iovine et al., 1995). The selective phase model of transport proposes that NTR binding catalyzes the local dissociation of the FG network to enable efficient passage of cargo (Schmidt and Görlich, 2016), and it has been suggested that NTR binding also prevents non-productive Nup interactions outside of pore complexes (Frey and Görlich, 2007; Schmidt and Görlich, 2015). NTRs have also been proposed to prevent assembly of specific Nups during mitosis (Harel et al., 2003; Walther et al., 2003), and to chaperone histones (Padavannil et al., 2019), mitotic spindle components

(Nachury et al., 2001), and intrinsically disordered RNA binding proteins including FUS and TDP-43 (Guo et al., 2018; Hofweber et al., 2018; Hutten et al., 2020).

NTRs are present at high concentrations in the cytoplasm and are relatively large proteins (~100-150 kD), thus their available binding surfaces make them good candidates for chaperones (Springhower et al., 2020). The crystal structure of a Nup214/CRM1 complex reveals that the Nup214 FG domain makes extensive contacts with hydrophobic patches on the surface of CRM1 (Port et al., 2015). Furthermore, CRM1 generates high affinity interactions with both Nup214 and Nup358 that are significantly stronger than the weak, transient interactions characteristic of most Nup/NTR pairs (Port et al., 2015; Ritterhoff et al., 2016; Tan et al., 2018). Both Nup214 and Nup358 are required for condensate formation in *C. elegans* oocytes, therefore stable interaction of these specific Nups with CRM1 likely suppresses condensation in the cytoplasm. Of note, the NTR transportin did not affect Nup solubility in *C. elegans* oocytes, suggesting that chaperoning behavior may be specific to CRM1.

Nup foci might not serve an essential biological role and are potentially toxic

Cytoplasmic Nup foci have been proposed to function in pore biogenesis in *Drosophila* oocytes (Hampoelz et al., 2019b), nuclear pore inheritance during cell division in yeast (Colombi et al., 2013), or as reservoirs of pre-formed pore complexes to support the rapid divisions of nuclei in cell culture and *Drosophila* embryos (Hampoelz et al., 2016; Ren et al., 2019). Our analyses do not support such roles for Nup foci in *C. elegans*. First, Nup foci account for only a very small proportion of FG-Nups (<3%) in oocytes, the vast majority of which exist in the cytoplasm as a soluble pool. Second, Nup foci are transient structures that dissolve fully at oocyte maturation and every M phase thereafter, making them unlikely to be a source of partially or fully assembled pore complexes. Third, we have characterized a mutant lacking Nup214, a non-essential FG-Nup, that is 100% viable despite lacking abundant Nup foci in oocytes and embryos. We suggest instead that Nup foci are “accidental” condensates that offer no benefits to cells and may in fact be precursors to toxic condensates. Aberrant condensation of Nup98 and Nup214 fusion proteins drives oncogenic transformation in certain types of leukemia (Chandra et al., 2022; Terlecki-Zaniewicz et al., 2021; Zhou and Yang, 2014) and Nups are often present in pathological inclusions in primary patient samples and models of neurodegenerative disease (Chandra and Lusk, 2022; Fallini et al., 2020; Hutten and Dormann, 2020). Our findings suggest that Nups are not merely passive clients of pathological inclusions but can initiate the formation of toxic condensates. Ectopically expressed Nup98 formed cytoplasmic condensates in neurons that recruited endogenous Nup62 away from the nuclear envelope and caused paralysis. Nup98 is highly cohesive due to its extreme hydrophobicity and interacts with Nups from multiple subcomplexes (Griffis et al., 2003; Onischenko et al., 2017; Yoshida et al., 2011); therefore Nup98 may be uniquely capable of seeding toxic condensates. Our findings are consistent with recent studies reporting that cytoplasmic FG-Nups drive aggregation of TDP-43 in both ALS/FTLD and following traumatic brain injury (Anderson et al., 2021; Gleixner et al., 2022).

The deleterious effects of Nup condensation are likely context dependent. In fully mature arrested oocytes, Nup condensation increases by ~14 fold over growing oocytes, yet is likely not damaging as the majority of arrested oocytes go on to form viable embryos when fertilized (Jud et al., 2008). Pore complexes and Nup condensates in oocytes and embryos are fully disassembled during M phase, allowing for a cycle of “renewal” with each cell division. We suggest that Nup condensation may only be dangerous in post-mitotic cells that lack M phase specific Nup solubilizers and where certain Nups are naturally long-lived (D’Angelo et al., 2009; Toyama et al., 2013).

In summary, the high propensity of FG-Nups to form multivalent networks is critical in establishing the nuclear pore permeability barrier but presents a danger if Nup condensation is allowed to occur outside of nuclear pores. Cells like oocytes that naturally accumulate and clear Nup condensates offer a powerful model to study the mechanisms that promote and reverse Nup condensation.

Materials and methods

C. elegans and yeast strains and culture

C. elegans were cultured using standard methods (Brenner, 1974). Briefly, worms were maintained at 20°C on normal nematode growth media (NNGM) plates (IPM Scientific Inc. cat # 11006-548) seeded with OP50 bacteria. We have found that Nup solubility is highly influenced by multiple factors including animal age: for all Nups tested the number and size of foci increased significantly between days 1 and 2 of adulthood (see Figure S2B). Therefore, for all experiments worms were synchronized as day 1 or 2 adults using vulval morphology to stage L4 larvae. The age of animals used for each experiment is indicated in figures and legends.

Endogenous *npp-21* (TPR) was tagged with GFP using CRISPR/Cas9-mediated genome editing as previously described (Arribere et al., 2014). Endogenous *npp-24* (Nup88) and *npp-2* (Nup85) were tagged with G>F>P using SapTrap CRISPR/Cas9 gene modification as previously described (Schwartz and Jorgensen, 2016). G>F>P contains Frt sites in introns 1 and 2 of GFP that enable FLP-mediated, conditional knockout; in the absence of FLP, the construct behaves as normal GFP. Endogenous *npp-19* (Nup35) was tagged with G>F>P based on protocols for nested CRISPR (Vicencio et al., 2019) and “hybrid” partially single-stranded DNA donors (Dokshin et al., 2018). All other endogenous edits were performed using CRISPR/Cas9-mediated genome editing as described previously (Paix et al., 2017). Transgenic Nup214 and Nup98 strains (JH4119 and JH4204) were generated using SapTrap cloned vectors as previously described (Fan et al., 2020). Standard crosses were used to generate strains with multiple genomic edits. All strains used or generated in this study are described in Table S1.

Yeast strains were generated using homologous recombination of PCR-amplified cassettes (Longtine et al., 1998). Endogenous *NUP159* (Nup214), *NUP60* (Nup153), and *NUP2* (Nup50) were tagged by amplifying the *mNeonGreen::HIS3* cassette from pFA6a-mNeonGreen::HIS3 (Thomas et al., 2019) using primers with homology to the C-termini (without the stop codon) and downstream regions of the genes. Yeast strains generated in this study are described in Table S1.

RNAi

RNAi was performed by feeding (Timmons and Fire, 1998). RNAi vectors were obtained from the Ahringer or Open Biosystems libraries and sequence verified, or alternatively cloned from *C. elegans* cDNA and inserted into the T777T enhanced RNAi vector (Addgene cat # 113082). RNAi feeding vectors were freshly transformed into HT115 bacteria, grown to log phase in LB + 100 µg/mL ampicillin at 37°C, induced with 5 mM IPTG for 45 min, and plated on RNAi plates (50 µg/mL Carb, 1 mM IPTG; IPM Scientific Inc. cat # 11006-529). Seeded plates were allowed to dry overnight at RT before adding L4 larvae or day 1 adults. For depletion of Nup98 (Figures 2B and S2C), RNAi feeding was performed for 6 hr at 25°C; partial depletion was used to minimize cytological defects caused by loss of Nup98. For all other experiments, RNAi feeding was performed for 18-24 hr at 25°C. For all experiments, control worms were fed HT115 bacteria transformed with the corresponding L4440 or T777T empty vector.

Immunofluorescence

For immunostaining of embryos, gravid adults were placed into 7 µL of M9 media on a poly-L-lysine coated slide and compressed with a coverslip to extrude embryos. For immunostaining of oocytes, staged adults were dissected on poly-L-lysine slides to extrude the germline, and a coverslip was placed gently on top. In both cases, slides were immediately frozen on aluminum blocks pre-chilled with dry ice. After > 5 min, coverslips were removed to permeabilize embryos (freeze-cracking), and slides were fixed > 24 hr in pre-chilled MeOH at -20°C. Slides were then incubated in pre-chilled acetone for 10 min at -20°C, and blocked in PBS-T (PBS, 0.1% Triton X-100, 0.1% BSA) for > 30 min at RT. Slides were then incubated overnight in primary antibody in a humid chamber at 4°C. Slides were washed 3 x 10 min in PBS-T at RT, incubated in secondary antibody for 2 hr in a humid chamber at RT, and washed 3 x 10 min in PBS-T at RT. Slides were then washed 1x in PBS before being mounted using Prolong Glass Antifade Mountant with NucBlue (Thermo Fisher cat # P36981). Primary antibodies were diluted as follows: mAb414 (1:1,000; Biolegend cat # 902907), αNup358 (1:250; Novus Biologicals cat # 48610002), αNup50 (1:250, Novus Biologicals cat # 48590002), αGlcNAc RL2 (1:100; Invitrogen cat # MA1-072), αNup96 (1:250, (Ródenas et al., 2012)), αNup153 (1:250, (Galy et al., 2003)), αOLLAS-L2 (1:50, Novus Biologicals cat # NBP1-06713). Secondary antibodies were diluted as follows: Cy3 Donkey αMouse IgG (1:200; Jackson cat # 715-165-151), AlexaFluor 488 Goat αRabbit IgG (1:200; Invitrogen cat # A-11034), AlexaFluor 568 Goat αRabbit IgG (1:200; Invitrogen cat # A-11011), Alexa Fluor 488 Goat αRat IgG (1:200; Invitrogen cat # A-11006), AlexaFluor 488 αGFP (1:500; Invitrogen cat # A-21311).

LMB and HXD treatment, and HaloTag and Hoechst labeling

For CRM1 inhibition, leptomycin B (LMB; Sigma cat # L2913) was diluted in OP50 bacteria to a final concentration of 500 ng/mL and seeded on NNGM plates. 10-20 day 1 adults were transferred to LMB or control vehicle plates and incubated at 20°C for 4 hr prior to imaging. For treatment of yeast with 1,6-hexanediol (HXD), log-phase yeast were pelleted, re-suspended in media containing 5% HXD (Acros Organics cat # 629-11-8), and allowed to grow for 10 min at 30°C prior to imaging.

For HaloTag labeling, Janelia Fluor 646 HaloTag Ligand (Promega cat # GA1121) was diluted in OP50 bacteria to a final concentration of 30 μM and seeded on NNGM plates. 10-20 day 1 adults were added and incubated without light at 20°C for 12-16 hrs prior to imaging. For Hoechst staining, Hoechst 33342 dye (Thermo Fisher cat # 62249) was diluted in OP50 bacteria to a final concentration of 200 μM and seeded on NNGM plates. 10-20 day 1 adults were added and incubated without light at 20°C for 12-16 hrs prior to imaging.

Embryonic viability and lifespan analysis

To measure embryonic viability, six day 1 adults were transferred to six NNGM plates (36 worms total) and allowed to lay embryos for 1 hr at 20°C. Adults were then removed and the number of embryos on each plate was counted. Embryos were then allowed to hatch, and the number of adults on each plate was counted after 3 days at 20°C. Viability counts were repeated in three independent experiments, and embryonic viability was measured as the number of surviving adults divided by the original number of embryos counted in each experiment.

To measure adult lifespan, 75 day 1 adults were transferred to five NNGM plates (15 worms per plate) and incubated at 20°C. Worms were scored daily and considered dead if they failed to move when prodded. Worms were transferred every 2 days to avoid progeny, and any worms that crawled off the plates were censored from analysis.

Swimming assay

To measure swimming behavior, 5-10 day 1 adults were transferred to a 33 mm culture dish (MatTek cat # P35G-1.5-14-C) containing 400 µL M9 media and immediately filmed using an Axiocam 208 color camera (Zeiss) mounted on a Stemi 508 Stereo Microscope (Zeiss). Swimming assays were performed at RT (~22°C). Movies were exported to ImageJ, and the number of body bends per minute was counted manually.

Imaging

For live imaging of germlines, five staged adults were transferred to the middle well of a 3-chambered slide (Thermo Fisher cat # 30-2066A) in 10 µL of L-15 medium (Thermo Fisher cat # 21-083-027) with 1 mM levamisole. 20 µm polystyrene beads (Bangs Laboratories Inc. cat # PS07003) were then added to support a coverslip (Marienfeld cat # 0107052). Germlines were imaged using an inverted Zeiss Axio Observer with CSU-W1 SoRa spinning disk scan head (Yokogawa), 1x/2.8x/4x relay lens (Yokogawa), and an iXon Life 888 EMCCD camera (Andor) controlled by Slidebook 6.0 software (Intelligent Imaging Innovations). To image entire germlines, a 20 µm Z stack (1 µm step size) was captured using a 63x-1.4NA objective (Zeiss) with the 1x relay lens. For high resolution images of oocytes, 3 µm Z stacks (0.1 µm step size) were acquired using the 63x-1.4NA objective with the 2.8x relay lens. As germline condensates are highly sensitive to imaging-induced stress (Elaswad et al., 2022), care was taken to avoid compression of germlines, and all animals were imaged only once and maintained on the slide for < 5 min.

For live imaging of embryos, five young adults were transferred to 10 µL of L-15 medium on a coverslip and dissected to release embryos. 20 µm polystyrene beads were then added to prevent compression, and the coverslip was inverted onto a microscope slide (Thermo Fisher cat # 12-550-403). Embryos were imaged as 15 µm Z stacks (1 µm step size), captured using the 63x-1.4NA objective with the 2.8x relay lens. For imaging fixed germlines and embryos, prepared slides were imaged as 15 µm Z stacks (0.5 µm step size), captured using the 63x-1.4NA objective with the 2.8x relay lens.

For live imaging of yeast, cells were grown overnight in synthetic dropout media (Thermo Fisher cat # DF0919-15-3) at 30ºC and imaged in log-phase (OD_{600} of ~0.5) at room temperature. Yeast were imaged as 6 µm Z stacks (0.5 µm step size), captured using the 63x-1.4NA objective with the 2.8x relay lens.

Images were exported from Slidebook software and further analyzed using ImageJ or Imaris image analysis software. For presentation in figures, images were processed using ImageJ, adjusting only the minimum/maximum brightness levels for clarity with identical leveling between all images in a figure panel. Images presented in figures are maximum intensity projections (10 µm for germlines, 15 µm for embryos, 6 µm for yeast) or single focal planes as indicated in the legends.

Image quantification

The overlap of GFP or mNeonGreen-tagged Nups with Nup62::wrmScarlet (Figure 1D) was measured using single focal planes exported to ImageJ. The Nup62::wrmScarlet micrograph was used to create a mask defining the nuclear envelope as well as cytoplasmic foci as individual regions of interest (ROIs). This mask was then applied to both the GFP/mNeonGreen Nup micrograph as well as the Nup62::wrmScarlet micrograph and the integrated density was measured within each ROI. To control for cytoplasmic background, the average cytoplasmic signal for the GFP/mNeonGreen Nup was multiplied by the area of each ROI, and the resulting value subtracted from integrated density for the GFP/mNeonGreen Nup. Background normalized GFP/mNeonGreen Nup values were divided by Nup62::wrmScarlet values to obtain the ratio of GFP/mNeonGreen Nup to Nup62::wrmScalet at each ROI.

To quantify the overlap of GFP::Nup88 with membranes (Figure 1E), Z stacks of oocytes expressing GFP::Nup88 and the HaloTag::HDEL reporter were manually scored into 3 categories: 1. Complete overlap (the entire Nup88 focus overlapped with

HaloTag::HDEL); 2. Partial overlap (the Nup88 focus partially overlapped or was directly adjacent to HaloTag::HDEL); 3. No overlap (the Nup88 focus did not directly contract membranes marked by HaloTag::HDEL).

To quantify the distribution of Nups in oocytes as well as total expression, Z stacks were exported to Imaris image analysis software. The "Surface" tool was first used to isolate the -3 and -4 oocyte from each germline. For each pair of -3 and -4 oocytes, the Surface tool was then used to isolate both nuclei and the "Spot" tool was used to isolate cytoplasmic foci. The percent of Nup present at the nuclear envelope/nucleoplasm was measured as the intensity sum for both nuclei divided by the total intensity sum of the oocytes. Similarly, the percent of Nup present in foci was measured as the intensity sum for all foci divided by the total intensity sum of the oocytes. Finally, the percent soluble Nup was defined as 100% minus the percentage of Nup in both nuclei and foci. Total Nup expression was measured as the intensity sum of the -3 and -4 oocytes normalized to volume. To control for autofluorescent background in all measurements, staged animals lacking fluorescent tags were imaged using identical imaging settings. The average intensity sum per volume was calculated for the -3 and -4 oocytes of germlines lacking fluorescent tags and subtracted from the intensity sum measured for oocytes with tagged Nups.

To quantify the distribution of Nups in embryos, Z stacks were exported to Imaris software. The Surface tool was used to isolate the entire embryo as well as all nuclei, and the Spot tool was used to isolate cytoplasmic foci. The percent of Nup at the nuclear envelope/nucleoplasm or foci was measured as the intensity sum of all nuclei or foci divided by the total intensity sum of the embryo, respectively. The percent soluble Nup was defined as 100% minus the percentage of Nup in nuclei and foci. For all measurements, embryos lacking fluorescent tags were used to control for autofluorescent background as described for oocytes.

The Y complex component Nup85 localizes to meiotic chromosomes, therefore a high percentage of Nup85 is present in the nucleoplasm. Therefore, line-scan analysis was used to measure the amount of GFP::Nup85 at the nuclear envelope (Figure 2B). Z stacks were exported to ImageJ and line traces were drawn to pass through the central plane of -3 and -4 oocyte nuclei as well as the image background. For each nucleus, the two peak values of the nuclear envelope rim were averaged and normalized to the image background. Line-scan analysis was also used to quantify depletion of endogenous Nups from the nuclear envelope in neurons expressing *rab-3p*::Nup98::mNeonGreen or *UPN*::Nup358::mCherry (Figures 6D and E). Line traces were drawn to pass through the central plane of nuclei identified by Hoechst staining. For each nucleus, the two peak values for the nuclear envelope rim were averaged and normalized to the average value of Nup in the nucleoplasm. To quantify TFEB::GFP accumulation in the nucleus (Figure S6E), line traces were drawn to pass through the cytoplasm as well as the nucleoplasm. The average intensity value for TFEB::GFP in the nucleus was then divided by the average value of the cytoplasm.

To quantify cytoplasmic levels of mNeonGreen::Nup358 in oocytes versus intestinal cells (Figure 6A), single focal planes capturing both the germline and intestine were exported into ImageJ. For each image, 3 ROIs in the -3 oocyte, -2 oocyte, and intestinal cell cytoplasm were measured, averaged, and normalized to the image background.

Statistical analysis

All statistical tests were performed using GraphPad Prism 9.2.0 software. For comparison of three or more groups, significance was determined using a one-way ANOVA. For comparison of two groups, significance was determined using an unpaired t-test. In all figures error bars represent 95% confidence intervals (CI). For all figures, ns indicates not significant; *, $P < 0.05$; **, $P < 0.01$; ***, $P < 0.001$; ****, $P < 0.0001$.

Acknowledgements

We thank all members of the Seydoux and Cochella Labs, Orna Cohen-Fix, and the Baltimore Worm Club for support and many helpful discussions. We thank Cristina Ayuso and Basma Taleb for assistance with *C. elegans* genome engineering, Madeline Cassani for generating strain JH3656, and the Fromme Lab for generously sharing yeast strains and plasmids. We thank the Chuang Lab for sharing the transportin::mNeonGreen strain and the Greenstein Lab for sharing the GFP::NDC1 strain. Several *C. elegans* strains were provided by the Caenorhabditis Genetics Center (CGC), which is supported by the National Institutes of Health Office of Research Infrastructure Programs (P40 OD010440). This work was funded by the Spanish State Research Agency (PID2019-105069GB-I00) and the National Institutes of Health (R37HD037047). L.T. is a postdoctoral fellow of the Life Sciences Research Foundation supported by the Howard Hughes Medical Institute. G.S. is an investigator of the Howard Hughes Medical Institute.

Competing interests

G.S. serves on the Scientific Advisory Board of Dewpoint Therapeutics, Inc. The other authors declare no competing interests.

Name	Description	Genotype	Additional information	Source
BN740	GFP::Nup88; mCherry::histone	G>F>P::npp-24 (bq15) lmn-1p::mCherry::his-58::pie-1utr (bqSi189) II	mCherry::histone from Gómez-Saldivar et al., 2016	This study
BN1018	GFP::Nup35; mCherry::histone	G>F>P::npp-19 (bq29) lmn-1p::mCherry::his-58::pie-1utr (bqSi189) II		This study
BN1062	TPR::GFP; mCherry::histone	npp-21::GFP (bq1) lmn-1p::mCherry::his-58::pie-1utr (bqSi189) II		This study
BN452	GFP::ELYS; mCherry::histone	GFP::mel-28 (bq5) III; lmn-1p::mCherry::his-58::pie-1utr (bqSi189) II		Gómez-Saldivar et al., 2016
BN69	GFP::Nup107; mCherry::histone	npp-5(tm3039)/mIn1 [mIs14 dpy-10(e128)] II; pie-1p::GFP::npp-5 (bqIs51) pie-1p::mCherry::his-58 (ltIs37) IV		Ródenas et al., 2012
JH3850	GFP::Nup85; mCherry::histone	G>F>P::npp-2 (bq38) I; lmn-1p::mCherry::his-58::pie-1utr (bqSi189) II		This study
JH3867	mNeonGreen::Nup98; mCherry::histone	mNeonGreen::npp-10 (ax4538) III; lmn-1p::mCherry::his-58::pie-1utr (bqSi189) II		This study
JH3938	mNeonGreen::Nup358; mCherry::histone	mNeonGreen::npp-9 (ax4540) III; lmn-1p::mCherry::his-58::pie-1utr (bqSi189) II		This study
JH3908	gp210::mNeonGreen; mCherry::histone	npp-12::mNeonGreen (ax4539) I; lmn-1p::mCherry::his-58::pie-1utr (bqSi189) II		This study
JH4201	Nup62::wrmScarlet	npp-11::wrmScarlet (ax4547) I		This study
JH3906	RanGAP::wrmScarlet	ran-2::wrmScarlet (ax4545) III		This study
JH4202	NDC1::wrmScarlet	npp-22::wrmScarlet (ax4549) V		This study
DG4557	GFP::NDC1	GFP::3xFLAG::npp-22 (tn1794) V		Huelgas-Morales et al., 2020
OCF22	mCherry::Nup54	pie-1p::mCherry::npp-1::pie-1utr (ocfIs5)		Joseph-Strauss et al., 2012
JH3872	Nup214::OLLAS	npp-14::OLLAS (ax4548) I		This study
JCP519	NXF1::eGFP	nxf-1(t2160) V; nxf-1p::nxf-1::3xFLAG::eGFP::nxf-1utr (jcpEx6)		Zheleva et al., 2019
JH4115	GFP::Nup88; Nup62::wrmScarlet	G>F>P::npp-24 (bq15) II; npp-11::wrmScarlet (ax4547) I	cross between BN740 and JH4201	This study
JH4128	GFP::ELYS; Nup62::wrmScarlet	GFP::mel-28 (bq5) III; npp-11::wrmScarlet (ax4547) I	cross between BN452 and JH4201	This study
JH4083	GFP::Nup85; Nup62::wrmScarlet	G>F>P::npp-2 (bq38) npp-11::wrmScarlet (ax4547) I	cross between JH3850 and JH4201	This study
JH3995	mNeonGreen::Nup98; Nup62::wrmScarlet	mNeonGreen::npp-10 (ax4538) III; npp-11::wrmScarlet (ax4547) I	cross between JH3867 and JH4201	This study
JH3986	mNeonGreen::Nup358; Nup62::wrmScarlet	mNeonGreen::npp-9 (ax4540) III; npp-11::wrmScarlet (ax4547) I	cross between JH3938 and JH4201	This study

JH4203	gp210::mNeonGreen; Nup62::wrmScarlet	npp-12::mNeonGreen (ax4539) npp-11::wrmScarlet (ax4547) I	cross between JH3908 and JH4201	This study
JH3849	GFP::Nup88; mCherry::histone; HaloTag::HDEL	G>F>P::npp-24 (bq15) lmn-1p::mCherry::his-58::pie-1utr (bqSi189) II; HaloTag::HDEL (egxSi126) I	HaloTag::HDEL from Fan et al., 2020	This study
JH3849	GFP::Nup88; mCherry::histone; fog-2(q71)	G>F>P::npp-24 (bq15) lmn-1p::mCherry::his-58::pie-1utr (bqSi189) II; fog-2(q71) V	cross between BN740 and fog-2(q71)	This study
JH3656	G3BP::RFP; fog-2(q71)	gtbp-1::tagRFP (ax5000) IV; fog-2(q71) V; meg-3::GFP (ax3054) X		This study
N2	C. elegans wild isolate			
RB653	OGT mutant	ogt-1(ok430) III		The C. elegans Deletion Mutant Consortium, 2012
RB1169	OGA mutant	oga-1(1207) X		The C. elegans Deletion Mutant Consortium, 2012
JH3859	GFP::Nup88; mCherry::histone; OGT mutant	G>F>P::npp-24 (bq15) lmn-1p::mCherry::his-58::pie-1utr (bqSi189) II; ogt-1(ok430) III	cross between BN740 and RB653	This study
JH3869	GFP::Nup88; mCherry::histone; OGA mutant	G>F>P::npp-24 (bq15) lmn-1p::mCherry::his-58::pie-1utr (bqSi189) II; oga-1(1207) X	cross between BN740 and RB1169	This study
OG1124	OGT::GFP	ogt-1::GFP (dr84) III		Urso et al., 2020
JH4076	Nup62::wrmScarlet; CDK1::GFP	npp-11::wrmScarlet (ax4547) I; cdk-1::GFP (neSi12) II	CDK1::GFP from Shirayama et al., 2012	This study
JH3955	CRM1::mNeonGreen; mCherry::histone	xpo-1::mNeonGreen (ax4542) V; lmn-1p::mCherry::his-58::pie-1utr (bqSi189) II		This study
IX4676	transportin::mNeonGreen	imb-2::mNeonGreen::3xFLAG (vy280) II		Alqadah et al., 2019
MAH240	TFEB::GFP	hlh-30p::hlh-30::GFP (sqIs17)		Lapierre, 2013
JH3886	Nup214Δ	npp-14Δ (ax4543) I		This study
RB1290	Nup214 mutant	npp-14(ok1389) I		The C. elegans Deletion Mutant Consortium, 2012
JH3937	mNeonGreen::Nup358; mCherry::histone; Nup214Δ	mNeonGreen::npp-9 (ax4540) III; lmn-1p::mCherry::his-58::pie-1utr (bqSi189) II; npp-14Δ (ax4543) I	cross between JH3938 and JH3886	This study
JH3912	GFP::Nup88; mCherry::histone; Nup214Δ	G>F>P::npp-24 (bq15) lmn-1p::mCherry::his-58::pie-1utr (bqSi189) II; npp-14Δ (ax4543) I	cross between BN740 and JH3886	This study

JH3919	RanGAP::wrmScarlet; mCherry::histone; Nup214Δ	ran-2::wrmScarlet (ax4545) III; npp-14Δ (ax4543) I	cross between JH3906 and JH3886	This study
JH3959	mNeonGreen::Nup358; gp210Δ	mNeonGreen::npp-9 (ax4540) III; npp-12Δ (ax4544) I		This study
JH4119	mex-5p::Nup214::wrmScarlet; mNeonGreen::Nup358	mex-5p::npp-14::wrmScarlet::ollas::tbb-2utr (ax4541) I; mNeonGreen::npp-9 (ax4540) III		This study
JH4204	rab-3p::Nup98::mNeonGreen; Nup62::wrmScarlet	rab-3p::npp-10(1-919)::mNeonGreen::tbb-2utr (ax4550); npp-11::wrmScarlet (ax4547) I		This study
JH4169	UPN::Nup358::mCherry; mNeonGreen::Nup98	UPN::npp-9::mCherry::blrp::3xFlag (otIs790); mNeonGreen::npp-10 (ax4538) III	UPN::Nup358::mCherry from Sun and Hobert, 2021	This study
LTY3	Nup214::mNeonGreen	*MATa ura3-52 his3-Δ200 leu2-3,112 lys2-801 trp1-Δ901 suc2-Δ9 nup159::mNeonGreen::HIS3*	Integration into SEY6210.1 (Robinson et al., 1988)	This study
LTY6	Nup153::mNeonGreen	*MATa ura3-52 his3-Δ200 leu2-3,112 lys2-801 trp1-Δ901 suc2-Δ9 nup60-mNeonGreen::HIS3*	Integration into SEY6210.1 Robinson et al., 1988)	This study
LTY8	Nup50::mNeonGreen	*MATa ura3-52 his3-Δ200 leu2-3,112 lys2-801 trp1-Δ901 suc2-Δ9 nup2-mNeonGreen::HIS3*	Integration into SEY6210.1 (Robinson et al., 1988)	This study

Table S1. *C. elegans* and yeast strains used or generated in this study.

Figure 1

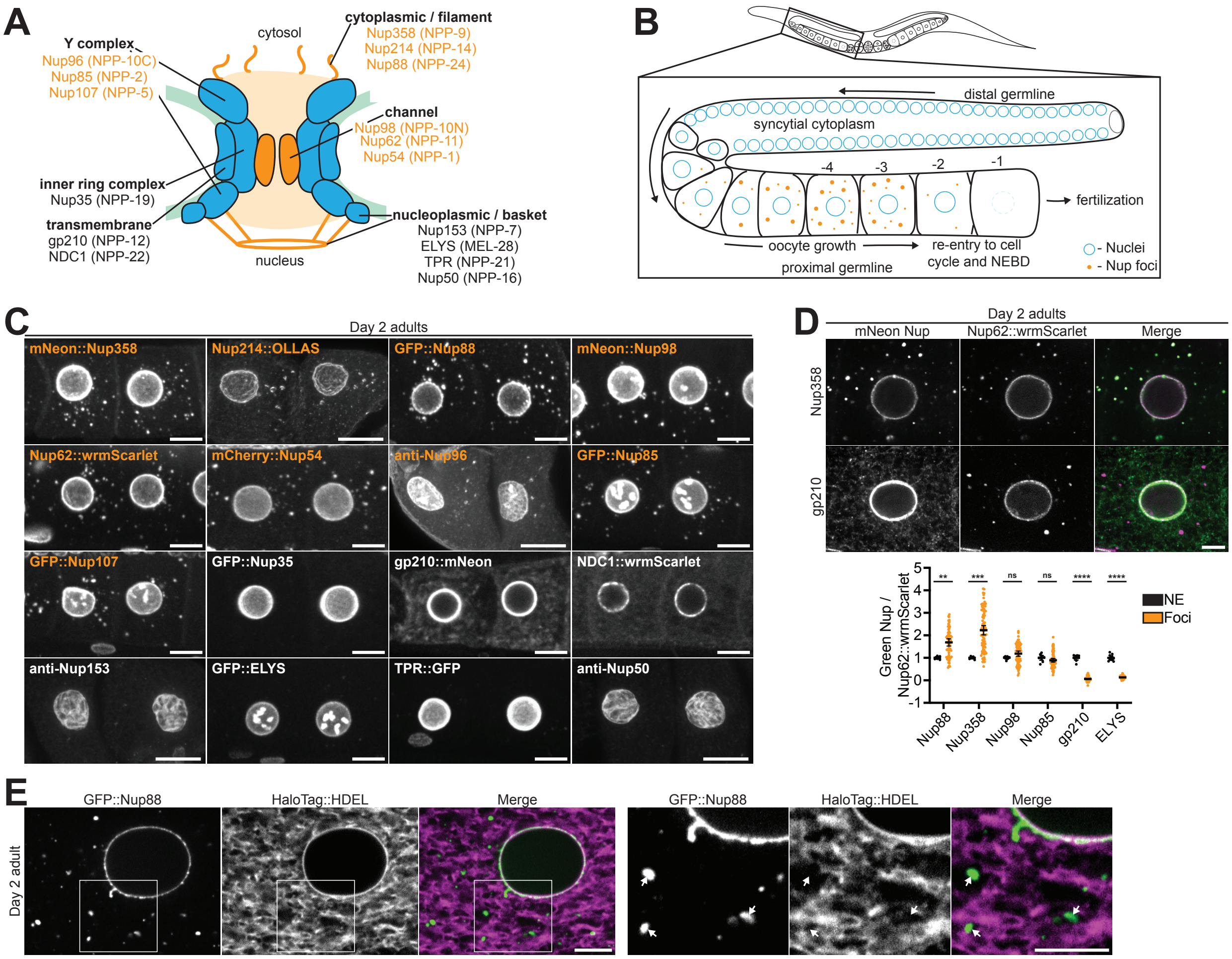

Figure 1. FG-Nups and their binding partners form cytoplasmic foci in *C. elegans* oocytes. A. Schematic depicting the structure of a nuclear pore complex, which consists of ~30 nucleoporin (Nup) proteins arranged in distinct subcomplexes. Blue subcomplexes are structural elements of the pore and include transmembrane Nups, the inner ring complex, and two copies of the Y complex. FG domain Nups are designated in orange and generate the permeability barrier of the central channel, and additionally localize to cytoplasmic filaments and the nuclear basket. Nups listed in orange localize to cytoplasmic foci in oocytes, whereas those denoted in black do not. Nups are listed with human names, with *C. elegans* homologs in parentheses. B. Schematic depicting Nup foci in the germline of a *C. elegans* adult hermaphrodite. Germ cell nuclei (designated in blue) proliferate in a syncytial cytoplasm before becoming

enclosed by membrane to form individual oocytes. Oocytes arrest in meiosis I and grow in an assembly line-like fashion until induced by sperm signaling to re-enter the cell cycle in preparation for fertilization. In young, wild-type *C. elegans*, Nup foci (designated in orange) are absent from the syncytial cytoplasm, and first appear in oocytes. Nup foci progressively accumulate, peaking in the -3 and -4 oocytes, before fully disassembling in the -1 oocyte prior to fertilization. C. Representative confocal micrographs of the -3 and -4 oocytes from Day 2 adult *C. elegans* expressing tagged versions of each indicated Nup, or stained with antibodies against endogenous Nups. All images are maximum intensity projections, with the exception of gp210 and NDC1 which are single imaging planes. Orange labels designate Nups enriched in cytoplasmic foci. D. Top: Representative confocal micrographs of Day 2 adult oocytes showing colocalization of CRISPR-tagged Nup62::wrmScarlet with mNeonGreen-tagged Nup358 or gp210. Bottom: Quantification of the overlap between Nup62::wrmScarlet and each indicated Nup at the nuclear envelope (NE) versus cytoplasmic foci. Each point designates an individual nucleus or focus. Values are normalized so that the average ratio at the nuclear envelope = 1.0. Error bars represent 95% CI for n > 7 (nuclei) or n > 59 (foci). E. Representative confocal micrographs showing overlap of CRISPR-tagged GFP::Nup88 with the luminal endoplasmic reticulum/nuclear envelope marker HaloTag::HDEL in a Day 2 adult oocyte. 20% of foci completely overlapped with HaloTag::HDEL, 64% partially overlapped, and 16% showed no overlap with HaloTag::HDEL (n = 118). Areas indicated by white boxes are magnified at right; white arrows indicate foci that do not completely overlap with the endoplasmic reticulum.

****, $P<0.0001$; ***, $P<0.001$; **, $P<0.01$; ns, not significant. Scale bars = 10 μm (panel C) or 5 μm (panels D and E).

Figure 2

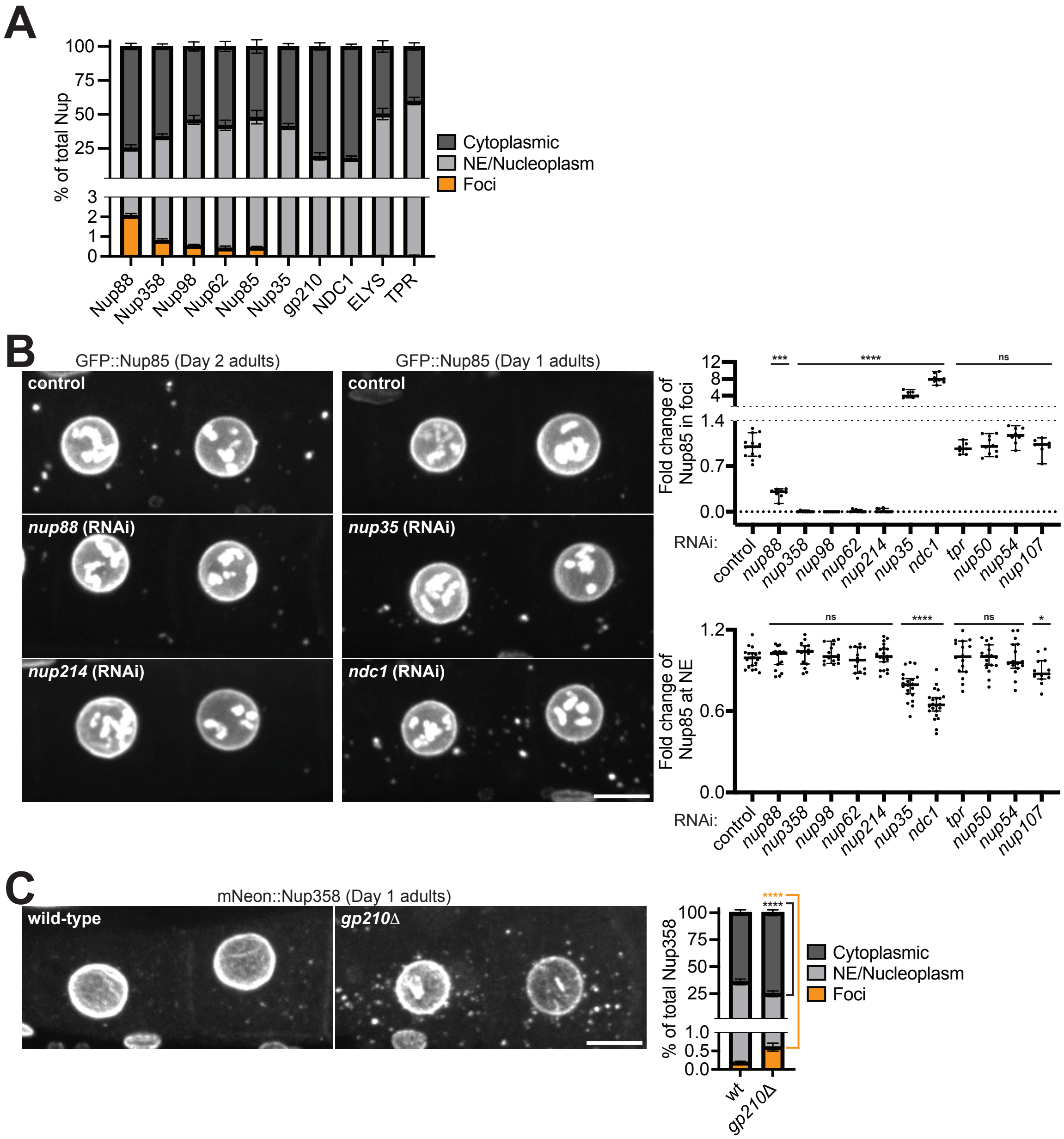

Figure 2. Nup foci are scaffolded by cytoplasmic facing FG-Nups. A. Quantification of the distribution of each designated Nup between the cytoplasm (soluble), nuclear envelope (NE)/nucleoplasm, and cytoplasmic foci. Measurements were made using the -3 and -4 oocytes of Day 2 adults. Error bars represent 95% CI for n > 5 germlines. B. Left: Representative confocal micrographs showing -3 and -4 oocytes of Day 1 or Day 2 adults with CRISPR-tagged GFP::Nup85. *nup214* RNAi is representative of a treatment that largely abolishes Nup foci, whereas Nup foci were partially diminished following

RNAi-mediated knockdown of Nup88. Both *nup35* and *ndc1* RNAi enhanced Nup foci. Top right: Quantification of the total percent of GFP::Nup85 in foci following each RNAi treatment. Values are normalized so that the average control measurement = 1.0. Error bars represent 95% CI for n > 7 germlines. Bottom right: Line-scan quantification measuring GFP::Nup85 signal at the NE following each RNAi treatment. Values are normalized so that the average control measurement = 1.0. Error bars represent 95% CI for n > 13 nuclei. C. Left: Representative confocal micrographs showing CRISPR-tagged mNeonGreen::Nup358 in -3 and -4 oocytes of Day 1 wild-type versus *gp210*Δ adults. Right: Quantification of the distribution of mNeonGreen::Nup358 between the cytoplasm, NE/nucleoplasm, and cytoplasmic foci in wild-type versus *gp210*Δ oocytes. Error bars represent 95% CI for n > 6 germlines.

****, P<0.0001; ***, P<0.001; *, P<0.05; ns, not significant. All images in this figure are maximum intensity projections. Scale bars = 10 µm.

Figure 3

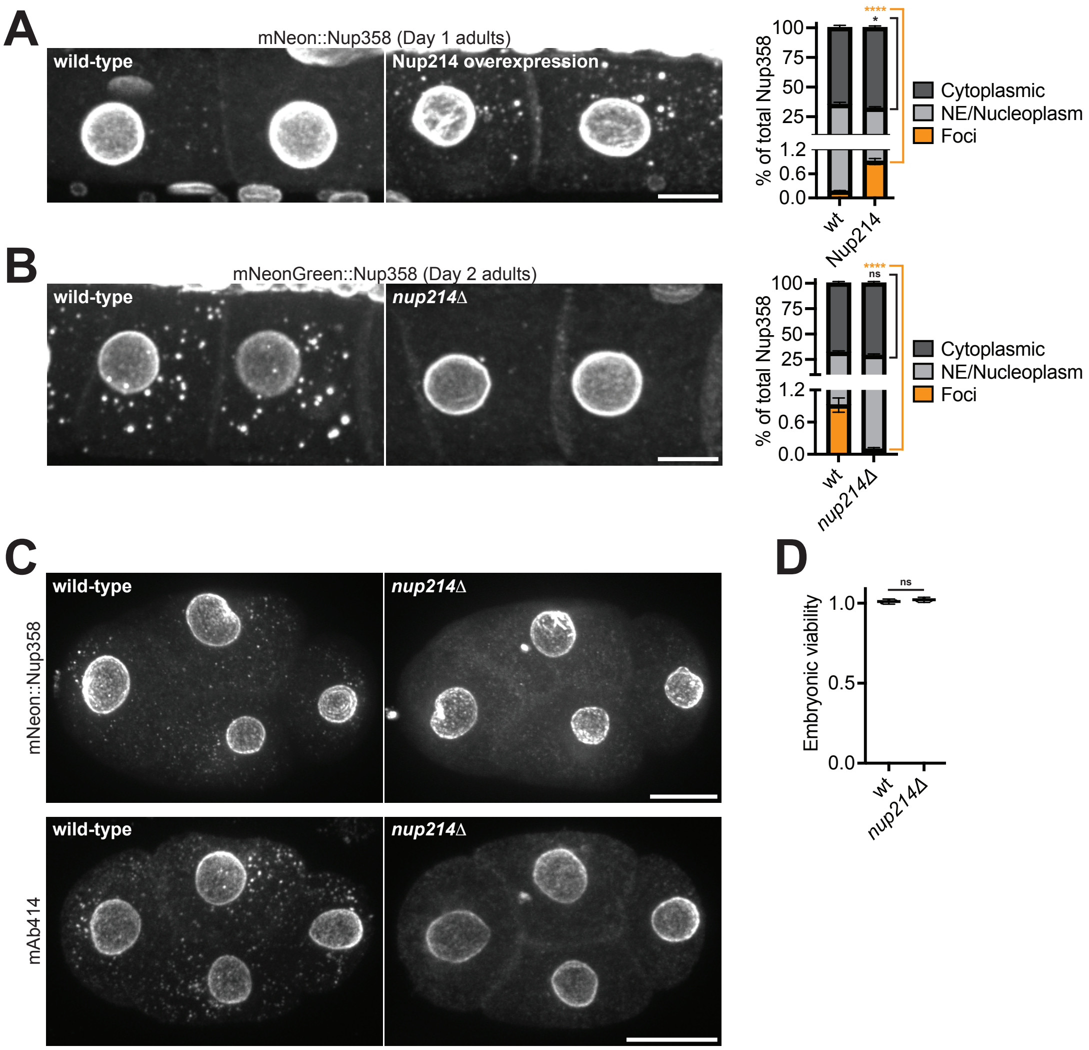

Figure 3. Nup214 is required for robust foci formation. A. Left: Representative confocal micrographs showing endogenous CRISPR-tagged mNeonGreen::Nup358 in -3 and -4 oocytes of Day 1 adults with or without overexpression of Nup214::wrmScarlet. Right: Quantification of the distribution of mNeonGreen::Nup358 between the cytoplasm, nuclear envelope (NE)/nucleoplasm, and cytoplasmic foci in wild-type oocytes versus those with Nup214 overexpression. Error bars represent 95% CI for n > 9 germlines. B. Left: Representative confocal micrographs showing mNeonGreen::Nup358 in -3 and -4 oocytes of wild-type versus *nup214Δ* Day 2 adults. Right: Quantification of the distribution of mNeonGreen::Nup358 between the cytoplasm

(soluble), NE/nucleoplasm, and cytoplasmic foci in wild-type versus *nup214Δ* oocytes. Error bars represent 95% CI for n > 8 germlines. C. Top: Representative confocal micrographs showing mNeonGreen::Nup358 in wild-type versus *nup214Δ* interphase 4-cell embryos. Bottom: Representative confocal micrographs showing endogenous Nups, visualized by mAb414, in wild-type versus *nup214Δ* 4-cell embryos. D. Embryonic viability of wild-type *C. elegans* versus the *nup214Δ* mutant. Error bars represent 95% CI for N = 3 independent experiments with n = 907 (wild-type) or n = 892 (*nup214Δ*) animals.

****, P<0.0001; *, P<0.05; ns, not significant. All images in this figure are maximum intensity projections. Scale bars = 10 µm.

Figure 4

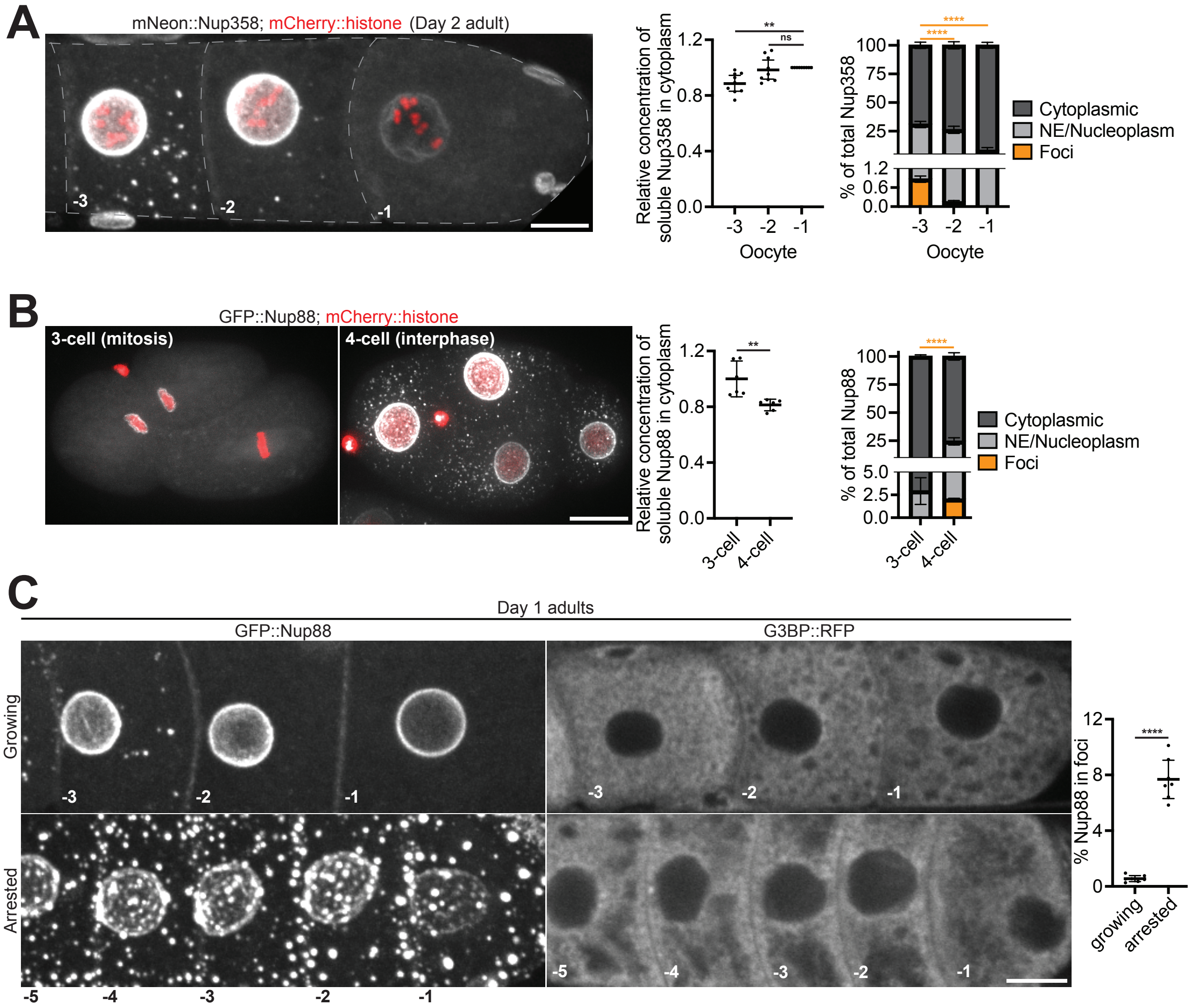

Figure 4. Nup solubility is regulated by cell cycle. A. Left: Representative confocal micrograph showing CRISPR-tagged mNeonGreen::Nup358 in Day 2 adult oocytes. Nup foci accumulate progressively throughout oocyte growth and peak in the -3 and -4 oocytes. Foci begin to disassemble in the -2 oocyte, and are absent from the -1 oocyte coincident with nuclear envelope breakdown. Middle: Cytoplasmic (soluble) mNeonGreen::Nup358 fluorescence normalized to volume in -1, -2, and -3 oocytes. Values are normalized within the same germline so that the -1 oocyte measurement = 1.0. Error bars represent 95% CI for n = 9 germlines. Right: Quantification of the distribution of mNeonGreen::Nup358 between the cytoplasm (soluble), nuclear

envelope (NE)/nucleoplasm, and cytoplasmic foci. Error bars represent 95% CI for n = 8 germlines. B. Left: Representative confocal micrographs of CRISPR-tagged GFP::Nup88 in 3-cell (mitosis) versus 4-cell (interphase) embryos. Middle: Cytoplasmic (soluble) GFP::Nup88 fluorescence normalized to volume in 3-cell mitotic embryos versus 4-cell interphase embryos. Values are normalized so that the average 3-cell embryo measurement = 1.0. Error bars represent 95% CI for n > 6 embryos. Right: Quantification of the distribution of GFP::Nup88 between the cytoplasm, NE/nucleoplasm, and cytoplasmic foci. Error bars represent 95% CI for n > 6 embryos. C. Left: Representative confocal micrographs showing GFP::Nup88 in the proximal germline of Day 1 adults of wild-type (growing) versus *fog-2(q71)* (arrested) oocytes, or CRISPR-tagged G3BP::RFP in mated (growing) versus unmated (arrested) *fog-2(q71)* oocytes. Right: Quantification of the percent of GFP::Nup88 in foci in wild-type versus *fog-2(q71)* oocytes. Error bars represent 95% CI for n > 7 germlines.

****, P<0.0001; **, P<0.01; ns, not significant. All images in this figure are maximum intensity projections, with the exception of G3BP (panel C) which are single focal planes. Scale bars = 10 µm.

Figure 5

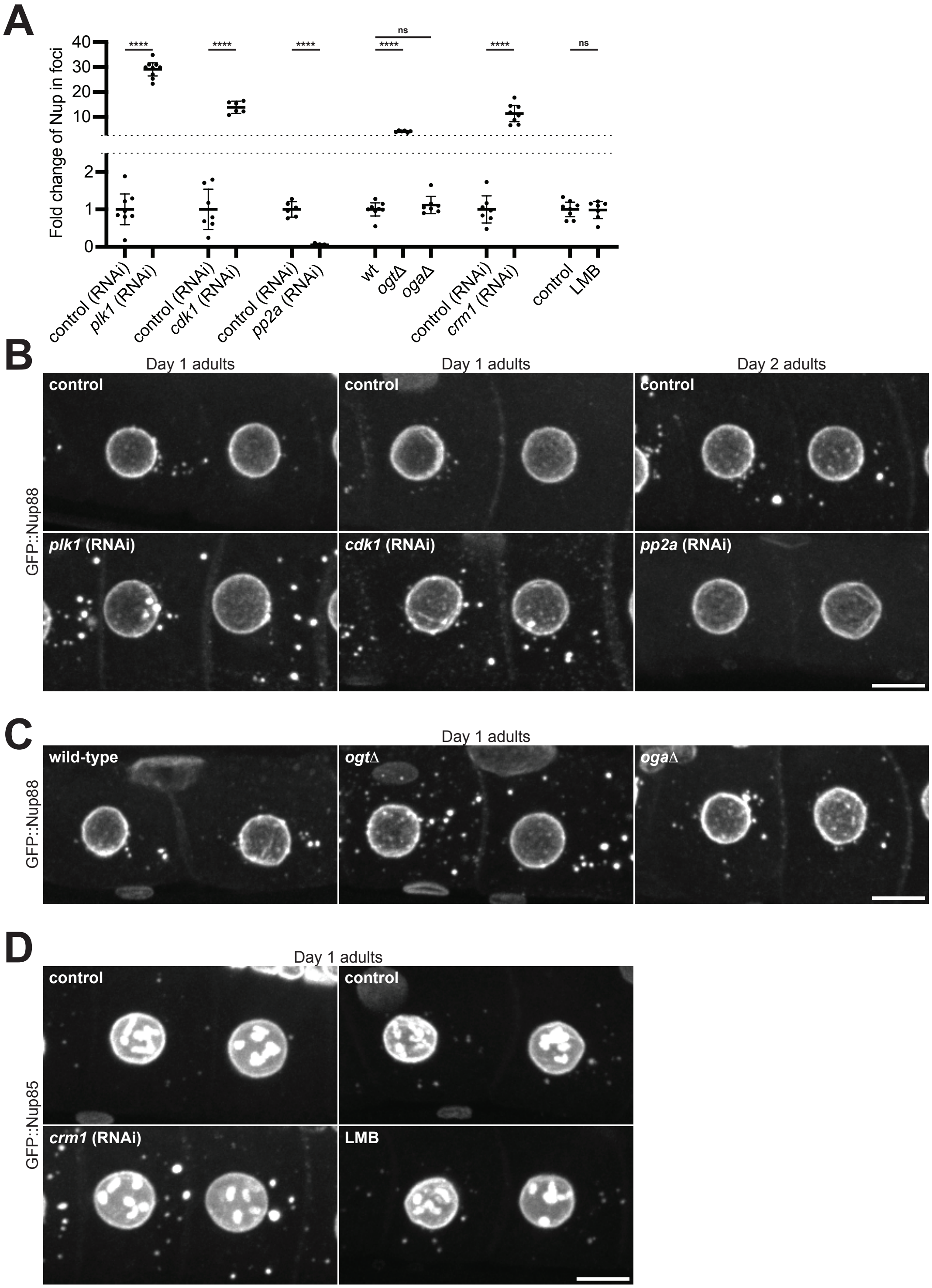
A
Fold change of Nup in foci
40
30
20
10
2
1
0
****
****
****
ns
****
****
ns
control (RNAi)
plk1 (RNAi)
control (RNAi)
cdk1 (RNAi)
control (RNAi)
pp2a (RNAi)
wt
ogtΔ
ogaΔ
control (RNAi)
crm1 (RNAi)
control
LMB
B
Day 1 adults
Day 1 adults
Day 2 adults
GFP::Nup88
control
control
control
plk1 (RNAi)
cdk1 (RNAi)
pp2a (RNAi)
C
Day 1 adults
GFP::Nup88
wild-type
ogtΔ
ogaΔ
D
Day 1 adults
GFP::Nup85
control
control
crm1 (RNAi)
LMB

Figure 5. Phosphorylation, GlcNAcylation, and CRM1 promote Nup solubility. A. Compiled quantification of the percent of Nup in foci in each indicated condition. Values are normalized so that the average control condition measurement = 1.0. Data correspond to micrographs in Figure 4B (*plk1* RNAi, n > 8 germlines; *cdk1* RNAi, n > 6 germlines; *pp2A* RNAi, n > 6 germlines), Figure 4C (*ogt*Δ and *oga*Δ mutants, n > 6 germlines), and Figure 4D (*CRM1* RNAi, n > 7 germlines; LMB treatment, n > 8 germlines). See Figure S5B for raw (non-normalized) values of the percent Nup in foci for each condition. B. Representative confocal micrographs showing CRISPR-tagged GFP::Nup88 in -3 and -4 oocytes depleted of PLK1, CDK1, or the PP2A scaffolding subunit PAA-1. Day 1 adults were used for kinase depletion, and Day 2 adults were used for phosphatase depletion. C. Representative confocal micrographs showing GFP::Nup88 in -3 and -4 oocytes of wild-type, *ogt*Δ, or *oga*Δ mutant Day 1 adults. D. Left: Representative confocal micrographs showing CRISPR-tagged GFP::Nup85 in -3 and -4 control oocytes or oocytes depleted of CRM1. Right: Representative confocal micrographs showing GFP::Nup85 in -3 and -4 oocytes of control animals or following treatment with the CRM1 inhibitor leptomycin b (LMB). All images are from Day 1 adults.

****, $P<0.0001$; ns, not significant. All images in this figure are maximum intensity projections. Scale bars = 10 μm.

Figure 6

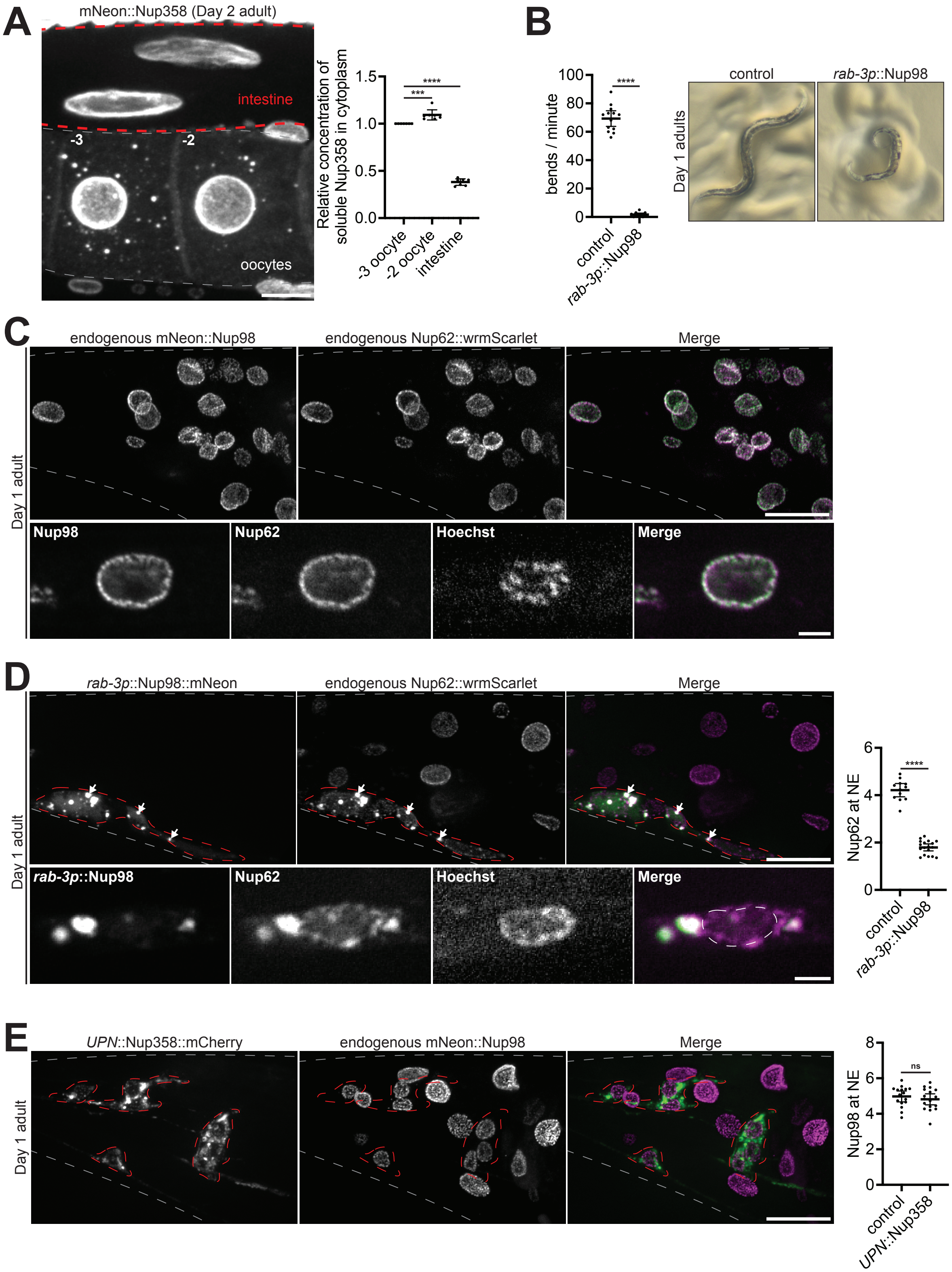
A
mNeon::Nup358 (Day 2 adult)
intestine
-3
-2
oocytes
Relative concentration of soluble Nup358 in cytoplasm
1.5
1.0
0.5
0.0
****
***
-3 oocyte
-2 oocyte
intestine
B
bends / minute
100
80
60
40
20
0
****
control
rab-3p::Nup98
Day 1 adults
control
rab-3p::Nup98
C
endogenous mNeon::Nup98
endogenous Nup62::wrmScarlet
Merge
Day 1 adult
Nup98
Nup62
Hoechst
Merge
D
rab-3p::Nup98::mNeon
endogenous Nup62::wrmScarlet
Merge
Day 1 adult
rab-3p::Nup98
Nup62
Hoechst
Merge
Nup62 at NE
6
4
2
0
****
control
rab-3p::Nup98
E
UPN::Nup358::mCherry
endogenous mNeon::Nup98
Merge
Day 1 adult
Nup98 at NE
8
6
4
2
0
ns
control
UPN::Nup358

Figure 6. Ectopic Nup98 foci deplete endogenous Nups from the nuclear envelope. A. Left: Representative confocal micrograph of CRISPR-tagged mNeonGreen::Nup358 in -2 and -3 oocytes and intestinal cells of a Day 2 adult. Red dashed lines denote intestinal cells, gray dashed lines outline oocytes. Right: Quantification of cytoplasmic (soluble) mNeonGreen::Nup358 signal in -3 oocytes, -2 oocytes, and intestinal cells. Values are normalized within the same animal so that the measurement for the -3 oocyte = 1.0. Error bars represent 95% CI for n = 7 animals. B. Left: Quantification of the swimming behavior of control Day 1 adults versus those with ectopically expressed Nup98::mNeonGreen driven by the pan-neuronal *rab-3* promoter. Error bars represent 95% CI for n > 11 worms. Right: Representative images of a control Day 1 adult versus a Day 1 adult expressing *rab-3p*::Nup98::mNeonGreen. C. Top: Representative confocal micrographs showing colocalization of CRISPR-tagged endogenous Nup62::wrmScarlet with CRISPR-tagged endogenous mNeonGreen::Nup98 in the tail of a Day 1 adult. Gray dashed lines indicate the boundary of the tail. Bottom: Representative confocal micrographs showing colocalization of endogenous Nup62 with Nup98 at a single nucleus. D. Top left: Representative confocal micrographs showing colocalization of endogenous Nup62::wrmScarlet with transgenic *rab-3p*::Nup98::mNeonGreen in the tail of a Day 1 adult. Gray dashed lines indicate the boundary of the tail. Note that transgenic *rab-3p*::Nup98::mNeonGreen is only expressed in neurons, which are designated by the red dashed outline. White arrows indicate colocalization of endogenous Nup62 with ectopic Nup98 foci. Bottom left: Representative confocal micrographs showing endogenous Nup62 depletion from the nuclear envelope. White dashed lines indicate the boundary of the nucleus. Right: Line-scan quantification of the nuclear envelope (NE) to nucleoplasm ratio of endogenous Nup62 in control (non-neuronal) cells, versus neurons with ectopically expressed *rab*-3p::Nup98::mNeonGreen. Error bars represent 95% CI for n > 12 nuclei. E. Left: Representative confocal micrographs showing colocalization of endogenous mNeonGreen::Nup98 with transgenic *UPN*::Nup358::mCherry in the tail of a Day 1 adult. Gray dashed lines indicate the boundary of the tail. Note that transgenic *UPN*::Nup358::mCherry is only expressed in neurons, which are designated by red dashed outlines. Right: Line-scan quantification of the NE to nucleoplasm ratio of

endogenous Nup98 in control (non-neuronal) cells, versus neurons with ectopically expressed *UPN*::Nup358::mCherry. Error bars represent 95% CI for n > 16 nuclei.

****, P<0.0001; ***, P<0.001; ns, not significant. All images in this figure are maximum intensity projections, with the exception of panels C and D (bottom) which are single focal planes. Scale bars = 2 μm (panels C and D, bottom) or 10 μm (all other panels).

Figure 7

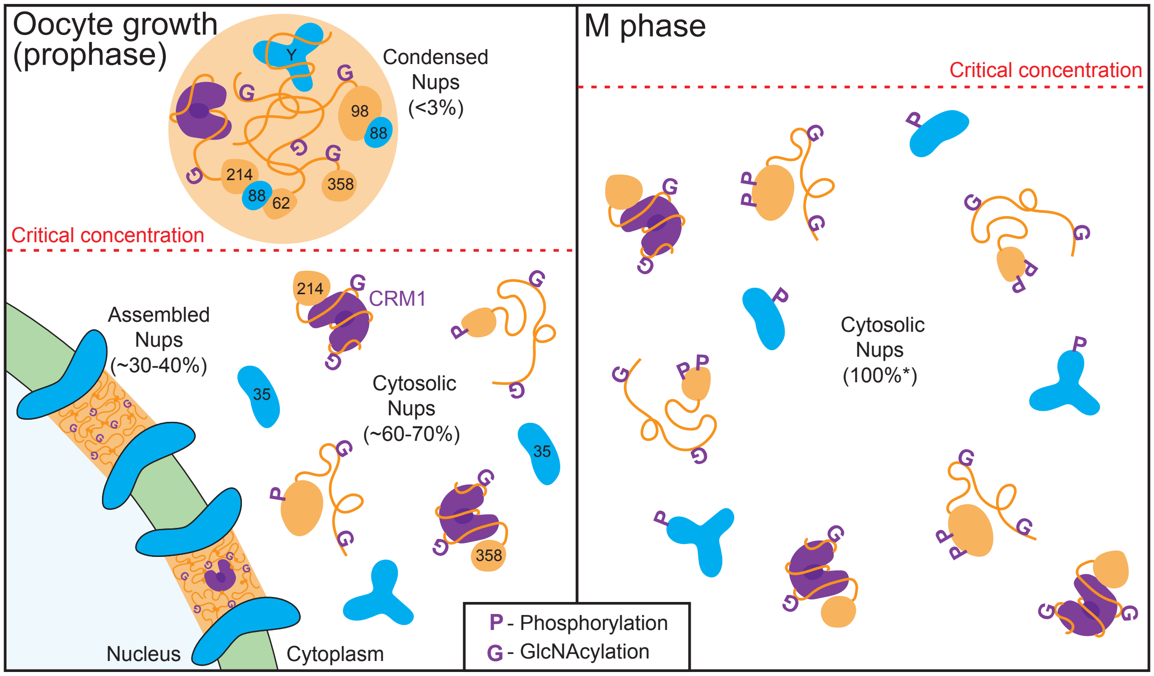

Figure 7. Multiple mechanisms regulate Nup solubility. Left: Nups are present at high concentrations in the cytoplasm of growing *C. elegans* oocytes. When Nup levels rise above the critical concentration, interactions among the FG-Nups Nup62, Nup98, Nup214, and Nup358 scaffold foci. Additionally, Nup88 contributes to foci formation by interacting with multiple FG-Nups. FG-Nup binding partners, including the Y complex, are recruited to foci as passive clients, whereas other Nups, including Nup35, are excluded from foci. In growing oocytes, only a minor fraction of Nups (<3%) is enriched in foci. Nups are maintained in a highly soluble state through multiple mechanisms including phosphorylation, GlcNAcylation of FG domains, and CRM1-mediated chaperoning (likely targeting the FG domains of Nup214 and Nup358). Note that the same mechanisms limit FG domain interactions within the central channel and drive nuclear pore disassembly during M phase. Right: During M phase, pore complexes as well as cytoplasmic Nup foci are disassembled and the concentration of soluble cytoplasmic Nups increases. Increased Nup solubility (thus a higher critical concentration) is largely driven by hyperphosphorylation mediated by cell cycle kinases

including PLK1 and CDK1. *Upon complete nuclear envelope breakdown, 100% of non-transmembrane or membrane-associated Nups become solubilized.

Figure S1

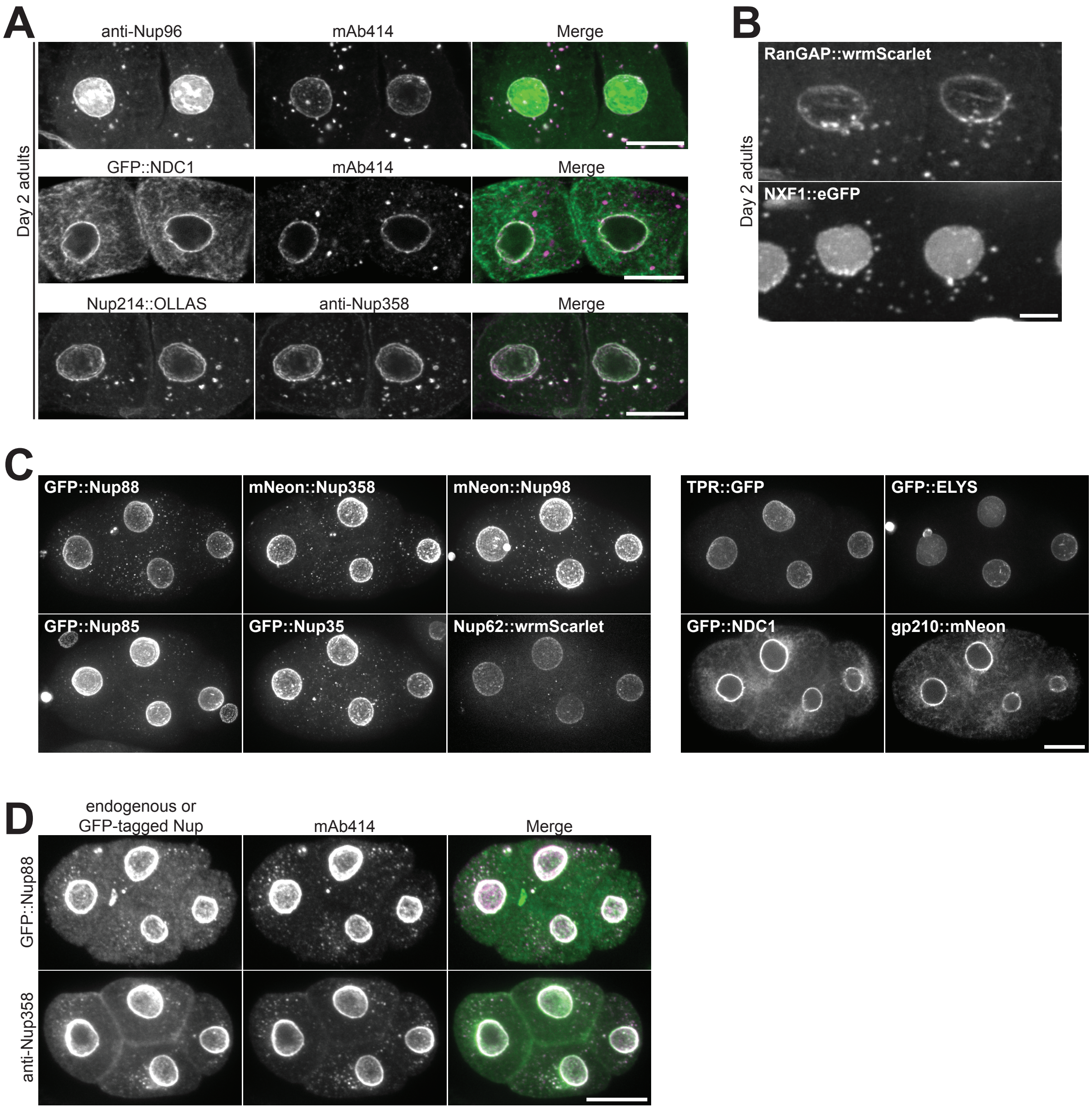

Figure S1. Nups form cytoplasmic foci in *C. elegans* early embryos. A. Top: Representative confocal micrographs depicting colocalization of endogenous Nup96 with mAb414 in Day 2 adult oocytes. Middle: Representative confocal micrographs depicting colocalization of CRISPR-tagged GFP::NDC1 with mAb414 in Day 2 adult oocytes. Bottom: Representative confocal micrographs showing colocalization of CRISPR-tagged Nup214::OLLAS with endogenous Nup358 in Day 2 adult oocytes. B.

Representative confocal micrographs of -3 and -4 oocytes from Day 2 adults expressing RanGAP::wrmScarlet or NXF1::eGFP. C. Representative confocal micrographs of interphase 4-cell embryos showing six Nups that localize to cytoplasmic foci (Nup88, Nup358, Nup98, Nup85, Nup35, and Nup62), and four Nups that are largely absent from foci (TPR, ELYS, NDC1 and gp210). D. Representative confocal micrographs depicting colocalization of CRISPR-tagged GFP::Nup88 or endogenous Nup358 with mAb414 in 4-cell embryos.

All images in this figure are maximum intensity projections, with the exception of NDC1 with mAb414 (panel A) and NDC1 and gp210 (panel C) which are single focal planes. Scale bars = 10 µm.

Figure S2

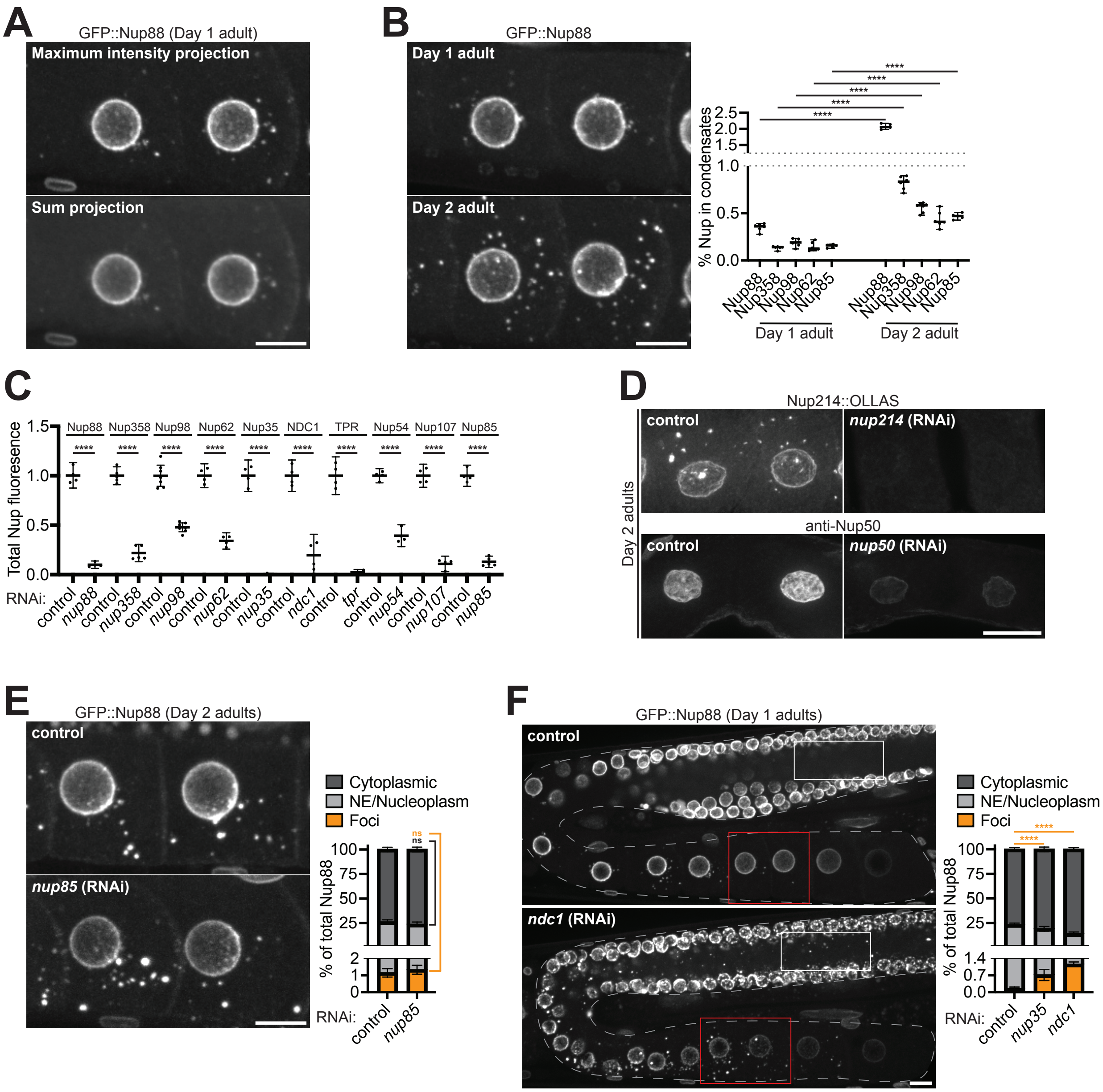

Figure S2. Controls for Nup RNAi experiments. A. Representative confocal micrographs showing -3 and -4 oocytes of a Day 1 adult with CRISPR-tagged GFP::Nup88. The 10 um Z stack is shown as a maximum intensity projection (top) or a sum projection (bottom). B. Left: Representative confocal micrographs showing -3 and -4 oocytes of Day 1 versus Day 2 adults expressing GFP::Nup88. Right: Quantification of the total percent of each indicated Nup in foci in Day 1 versus Day 2 adults. Error bars represent 95% CI for n > 5 germlines. Day 2 adult data is repeated from Figure 2A. C.

Quantification of the extent of RNAi-mediated depletion of each indicated Nup. Values are normalized so that the average control measurement = 1.0. Error bars represent 95% CI for n > 4 germlines. D. Representative confocal micrographs showing depletion of Nup214::OLLAS or endogenous Nup50 following *nup214* or *nup50* RNAi, respectively. E. Left: Representative confocal micrographs showing -3 and -4 oocytes of Day 2 adults with GFP::Nup88 as a marker for foci formation, with control RNAi or following depletion of Nup85. Right: Quantification of the distribution of GFP::Nup88 between the cytoplasm (soluble), nuclear envelope (NE)/nucleoplasm, and cytoplasmic foci in control oocytes versus those depleted of Nup85. Error bars represent 95% CI for n = 6 germlines. F. Left: Representative confocal micrographs of Day 1 adult germlines expressing GFP::Nup88 with control RNAi or following depletion of NDC1. White boxes denote the syncytial cytoplasm; foci are absent in control germlines but accumulate following depletion of NDC1. Red boxes indicate the -3 and -4 oocytes used for quantification. Right: Quantification of the distribution of GFP::Nup88 between the cytoplasm, NE/nucleoplasm, and cytoplasmic foci in control oocytes versus those depleted of Nup35 or NDC1. Error bars represent 95% CI for n > 5 germlines.

****, $P<0.0001$; ns, not significant. All images in this figure are maximum intensity projections. Scale bars = 10 μm.

Figure S3

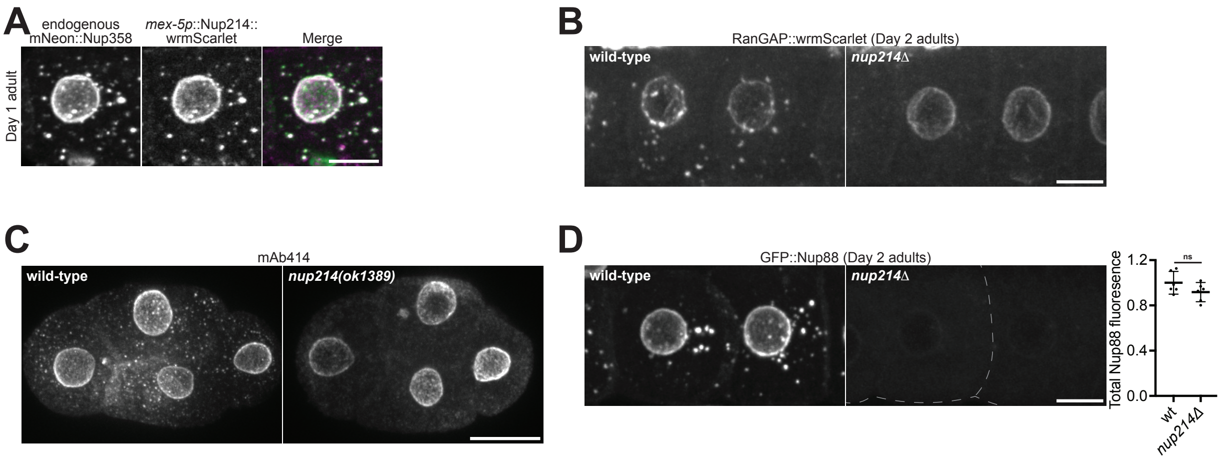

Figure S3. Nup88 requires Nup214 for recruitment to pore complexes. A. Representative confocal micrographs showing colocalization of endogenous mNeonGreen::Nup358 with Nup214::wrmScarlet overexpressed using the *mex-5* promoter. B. Representative confocal micrographs showing CRISPR-tagged RanGAP::wrmScarlet in -3 and -4 oocytes of wild-type versus *nup214*Δ Day 2 adults. C. Representative confocal micrographs showing endogenous Nups, visualized by mAb414, in wild-type versus *nup214(ok1389)* 4-cell embryos. D. Left: Representative confocal micrographs showing CRISPR-tagged GFP::Nup88 in -3 and -4 oocytes of wild-type versus *nup214*Δ Day 2 adults. Right: Quantification of total GFP::Nup88 fluorescence in wild-type versus *nup214*Δ oocytes. Values are normalized so that the average wild-type measurement = 1.0. Error bars represent 95% CI for n = 6 germlines.

ns, not significant. All images in this figure are maximum intensity projections. Scale bars = 10 μm.

Figure S4

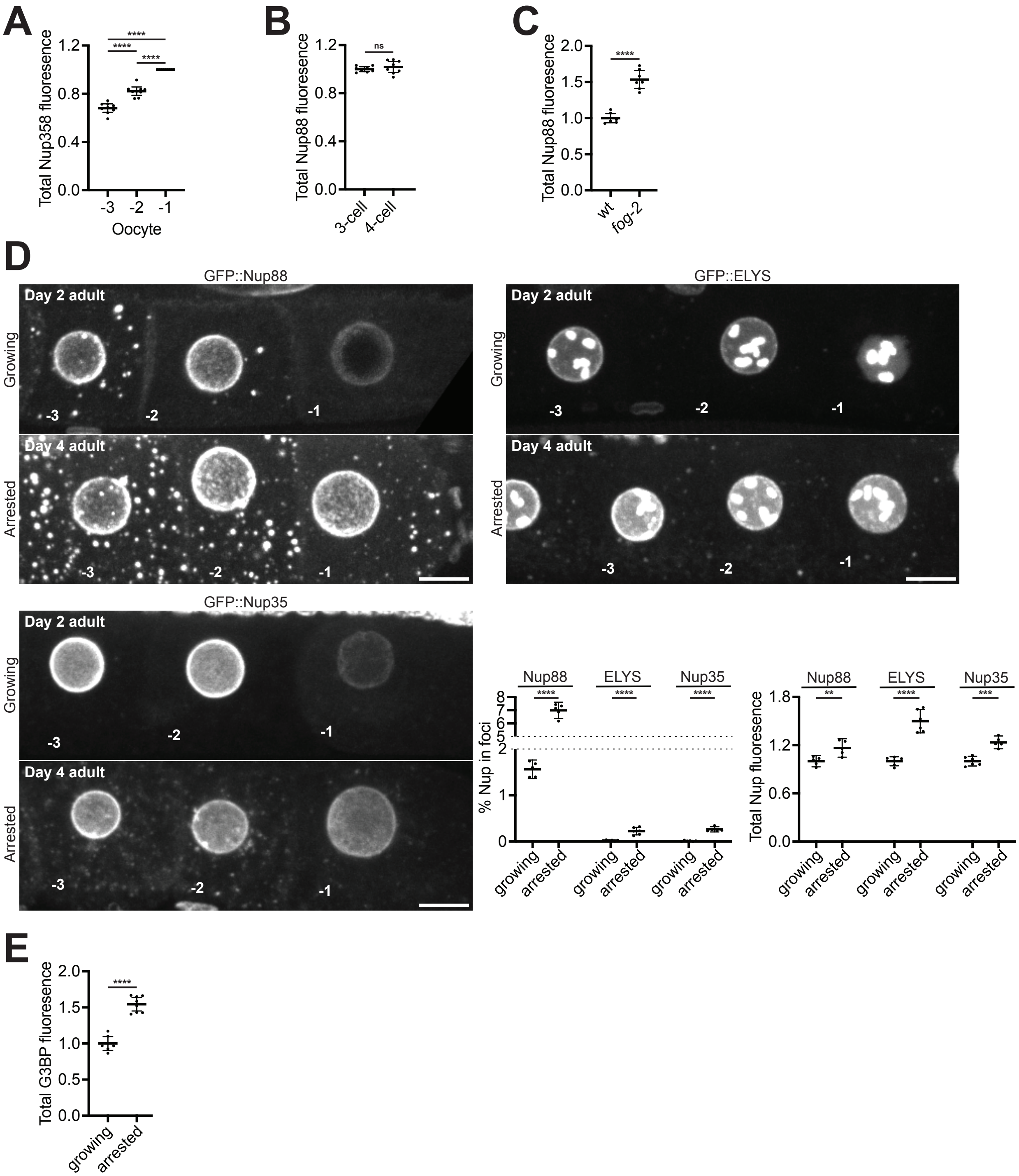

Figure S4. Nup foci formation is significantly increased in arrested oocytes. A. Quantification of total mNeonGreen::Nup358 fluorescence in -3, -2, and -1 oocytes. Values are normalized within the same germline so that the -1 oocyte measurement =

1.0. Error bars represent 95% CI for n = 9 germlines. B. Quantification of total GFP::Nup88 fluorescence in 3-cell (mitosis) versus 4-cell (interphase) embryos. Values are normalized so that the average fluorescence of 3-cell embryos = 1.0. Error bars represent 95% CI for n > 6 embryos. C. Quantification of total GFP::Nup88 fluorescence in wild-type versus *fog-2(q71)* arrested oocytes. Values are normalized so that the average fluorescence of wild-type = 1.0. Error bars represent 95% CI for n = 7 germlines. D. Top and bottom left: Representative confocal micrographs showing the proximal germline of Day 2 adults (growing oocytes) versus Day 4 adults (arrested oocytes) with CRISPR-tagged GFP::Nup88, GFP::ELYS, or GFP::Nup35. Bottom middle: Quantification of the total percent of each designated Nup in foci in Day 2 versus Day 4 adult oocytes. Error bars represent 95% CI for n > 5 germlines. Bottom right: Quantification of the total fluorescence of each designated Nup in Day 2 versus Day 4 adult oocytes. Values are normalized so that the average fluorescence of Day 2 adults = 1.0. Error bars represent 95% CI for n > 5 germlines. E. Quantification of the total G3BP::RFP fluorescence in mated (growing) versus unmated (arrested) *fog-2(q71)* oocytes. Values are normalized so that the average fluorescence of mated oocytes = 1.0. Error bars represent 95% CI for n > 7 germlines.

****, P<0.0001; ***, P<0.001; **, P<0.01; ns, not significant. All images in this figure are maximum intensity projections. Scale bars = 10 μm.

Figure S5

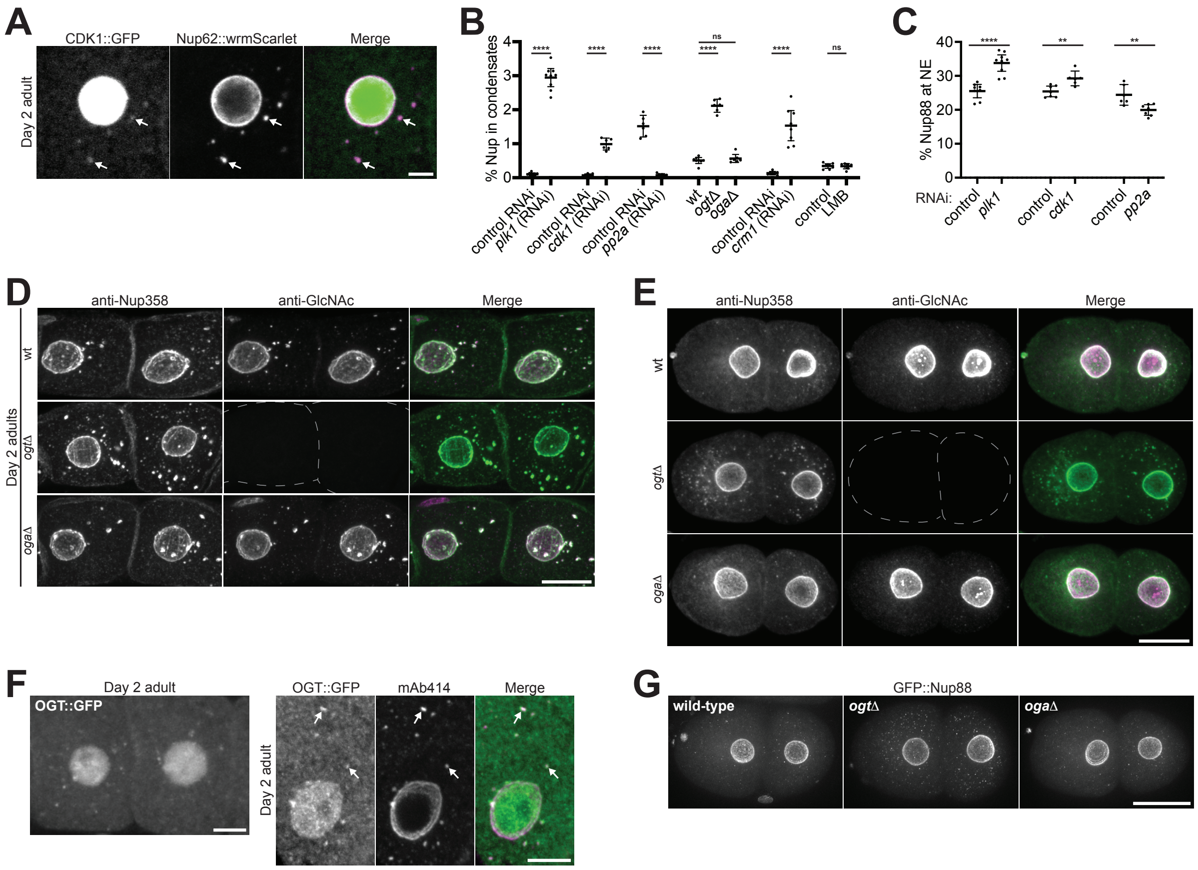

Figure S5. CDK1 and OGT localize to Nup foci and regulate Nup solubility. A. Representative confocal micrographs showing colocalization of endogenous Nup62::wrmScarlet with CDK1::GFP in a Day 2 adult oocyte. White arrows indicate overlap of CDK1 at Nup foci. B. Compiled quantification of the percent of Nup in foci in each indicated condition. Data correspond to micrographs in Figure 5B (*plk1* RNAi, n > 8 germlines; *cdk1* RNAi, n > 6 germlines; *pp2a* RNAi, n > 6 germlines), Figure 5C (*ogt*Δ and *oga*Δ mutants, n > 6 germlines), and Figure 5D (*CRM1* RNAi, n > 7 germlines; LMB treatment, n > 8 germlines). C. Compiled quantification of the percent of GFP::Nup88 at the nuclear envelope (NE) under each indicated condition. Data correspond to micrographs in Figure 5B (*plk1* RNAi, n > 8 germlines; *cdk1* RNAi, n > 6 germlines; *pp2a* RNAi, n > 6 germlines). D. Representative confocal micrographs showing colocalization of endogenous Nup358 with the RL2 GlcNAc antibody in wild-type, *ogt*Δ, or *oga*Δ Day 2 adult oocytes. E. Representative confocal micrographs showing colocalization of endogenous Nup358 with the RL2 GlcNAc antibody in wild-type, *ogt*Δ, or *oga*Δ interphase 2-cell embryos. F. Left: Representative confocal micrograph showing CRISPR-tagged OGT::GFP in -3 and -4 oocytes of a Day 2 adult. Right: Colocalization of OGT::GFP with mAb414 in a Day 2 adult oocyte. White arrows indicate overlap of OGT and mAb414 in cytoplasmic foci. G. Representative confocal micrographs showing CRISPR-tagged GFP::Nup88 in wild-type, *ogt*Δ, or *oga*Δ 2-cell embryos.

****, $P<0.0001$; **, $P<0.01$; ns, not significant. All images in this figure are maximum intensity projections. Scale bars = 5 µm (panel A and panel F, right) or 10 µm (all other panels).

Figure S6

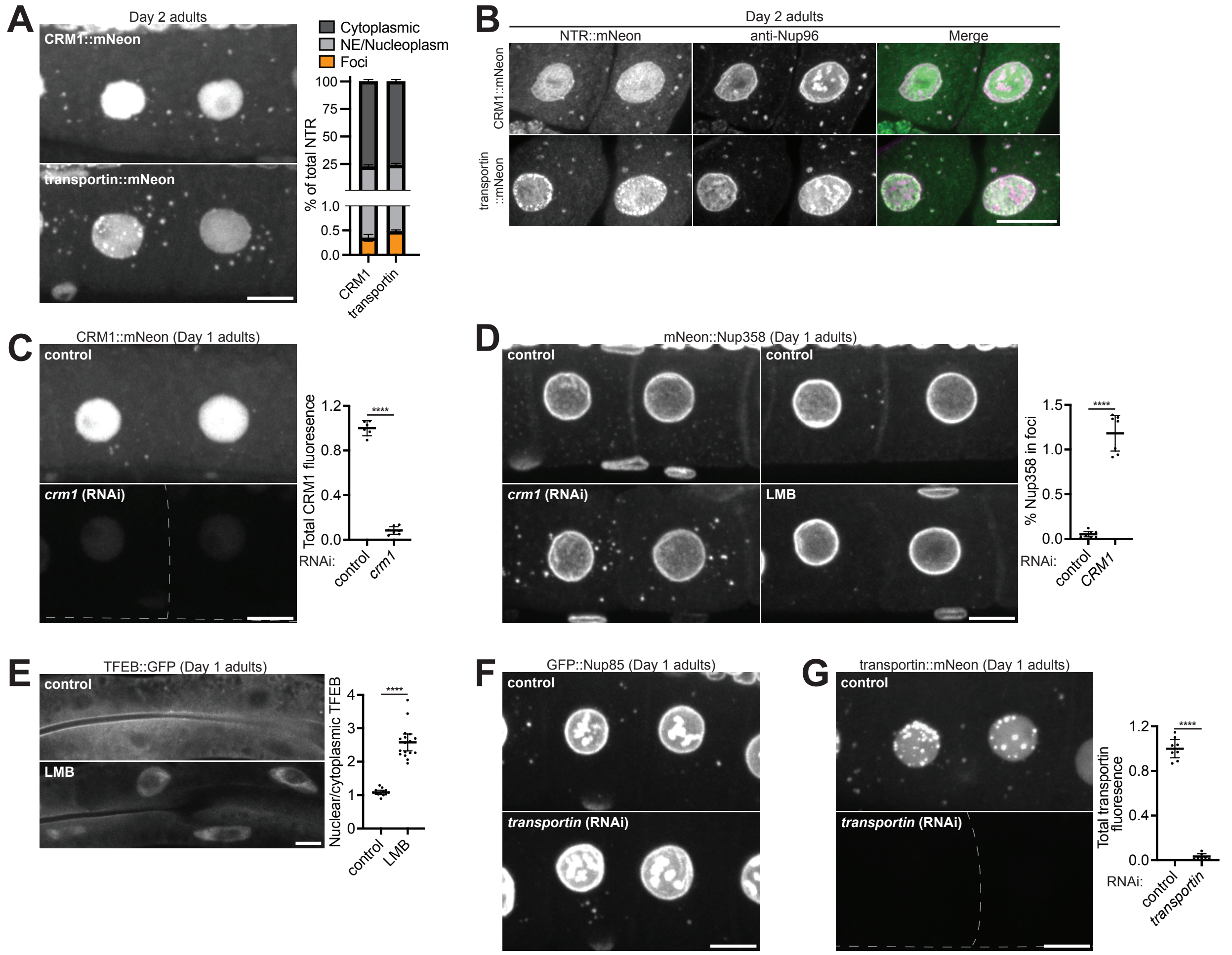

Figure S6. CRM1 and transportin localize to cytoplasmic Nup foci. A. Left: Representative confocal micrographs showing CRISPR-tagged CRM1::mNeonGreen or transportin::mNeonGreen in -3 and -4 oocytes of Day 2 adults. Right: Quantification of the distribution of CRM1::mNeonGreen and transportin::mNeonGreen between the cytoplasm (soluble), nuclear envelope (NE)/nucleoplasm, and cytoplasmic foci. Error bars represent 95% CI for n = 8 germlines. B. Representative confocal micrographs showing colocalization of CRM1::mNeonGreen and transportin::mNeonGreen with endogenous Nup96 in Day 2 adult oocytes. C. Left: Representative confocal micrographs showing CRM1::mNeonGreen in control -3 and -4 oocytes of Day 1 adults or oocytes targeted by *crm1* RNAi. Right: Quantification of total CRM1::mNeonGreen fluorescence in control oocytes or oocytes targeted by *crm1* RNAi. Values are normalized so that the average control measurement = 1.0. Error bars represent 95% CI for n > 6 germlines. D. Left: Representative confocal micrographs showing CRISPR-tagged mNeonGreen::Nup358 in control -3 and -4 oocytes of Day 1 adults or oocytes depleted of CRM1. Middle: Representative confocal micrographs showing mNeonGreen::Nup358 in control oocytes or following treatment with the CRM1 inhibitor leptomycin b (LMB). Right: Quantification of the total percent of mNeonGreen::Nup358 in foci in control oocytes or following CRM1 depletion. Error bars represent 95% CI for n > 7 germlines. E. Left: Representative confocal micrographs showing TFEB::GFP in control Day 1 adults or following LMB treatment. Right: Quantification of the nuclear/cytoplasmic ratio of TFEB::GFP in control cells or following LMB treatment; note that nuclear export of TFEB is mediated by CRM1 (Silvestrini et al., 2018). Error bars represent 95% CI for n > 13 nuclei. F. Representative confocal micrographs showing CRISPR-tagged GFP::Nup85 in -3 and -4 oocytes of control Day 1 adults or oocytes depleted of transportin. G. Left: Representative confocal micrographs showing transportin::mNeonGreen in control -3 and -4 oocytes of Day 1 adults or oocytes targeted by *transportin* RNAi. Right: Quantification of total transportin::mNeonGreen fluorescence in control oocytes or oocytes targeted by *transportin* RNAi. Values are normalized so that the average control measurement = 1.0. Error bars represent 95% CI for n > 7 germlines.

****, P<0.0001. All images in this figure are maximum intensity projections, with the exception of panel E which are single imaging planes. Scale bars = 10 μm.

Figure S7

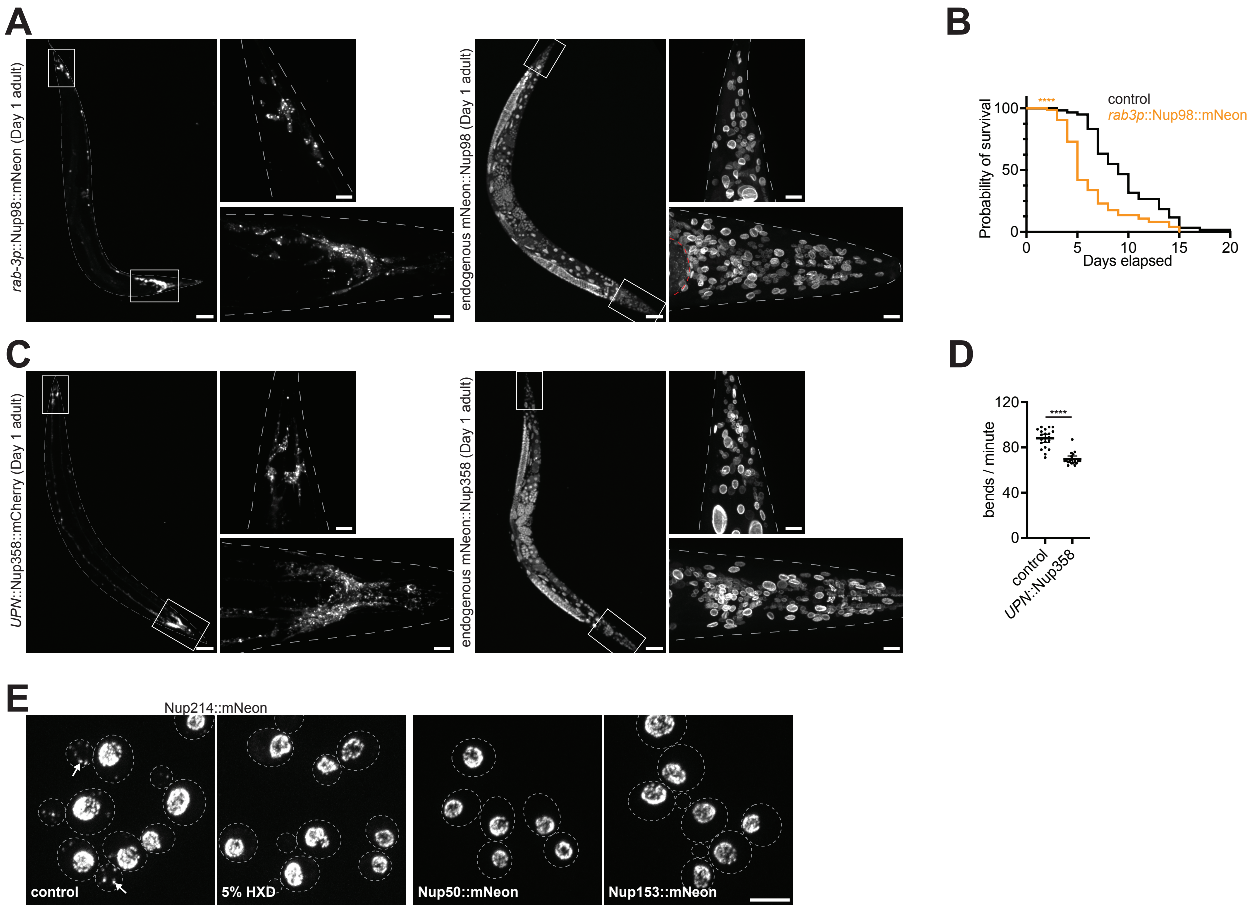

Figure S7. Ectopic Nup98 condensation in neurons is deleterious. A. Left: Representative confocal micrographs showing transgenic *rab-3p*::Nup98::mNeonGreen in a Day 1 adult *C. elegans.* The head and tail ganglia indicated by white boxes are magnified in the panels to the right. Right: Representative confocal micrographs showing endogenous CRISPR-tagged mNeonGreen::Nup98 in a Day 1 adult *C. elegans.* The head and tail indicated by white boxes are magnified in the panels to the right. Red dashes outline part of the germline. B. Survival curve of control *C. elegans* versus those with ectopically expressed *rab-3p*::Nup98::mNeonGreen. Error bars represent 95% CI for n = 61 (control) or n = 74 (*rab-3p*::Nup98::mNeonGreen) animals. C. Left: Representative confocal micrographs showing transgenic *UPN*::Nup358::mCherry in a Day 1 adult *C. elegans.* The head and tail ganglia indicated by white boxes are magnified in the panels to the right. Right: Representative confocal micrographs showing endogenous CRISPR-tagged mNeonGreen::Nup358 in a Day 1 adult *C. elegans.* The head and tail indicated by white boxes are magnified in the panels to the right. D. Quantification of the swimming behavior of control Day 1 adults versus those with ectopically expressed Nup358::mCherry driven by the pan-neuronal *UPN* promoter. Error bars represent 95% CI for n > 18 worms. E. Representative confocal micrographs showing endogenous Nup214, Nup50, and Nup153 tagged with mNeonGreen in yeast. Cells expressing Nup214::mNeonGreen were treated with 5% 1,6-hexandiol (HXD) for 10 min prior to imaging. White arrows denote cytoplasmic Nup foci.

****, $P<0.0001$. All images in this figure are maximum intensity projections. Scale bars = 100 µm (panels A and C, whole worms), 10 µm (panels A and C, head and tail magnification), or 5 µm (panel E).

Video S1. Swimming assay with control Day 1 adults lacking *rab-3p*::Nup98::mNeonGreen.

Video S2. Swimming assay with Day 1 adults expressing *rab-3p*::Nup98::mNeonGreen.

Video S3. Swimming assay with control Day 1 adults lacking *UPN*::Nup358::mCherry.

Video S4. Swimming assay with Day 1 adults expressing *UPN*::Nup358::mCherry.

References

Alberti, S., Gladfelter, A., and Mittag, T. (2019). Considerations and Challenges in Studying Liquid-Liquid Phase Separation and Biomolecular Condensates. Cell *176*, 419–434.

Alqadah, A., Hsieh, Y.W., Xiong, R., Lesch, B.J., Chang, C., and Chuang, C.F. (2019). A universal transportin protein drives stochastic choice of olfactory neurons via specific nuclear import of a sox-2-activating factor. Proc. Natl. Acad. Sci. *116*, 25137-25146.

Anderson, E.N., Morera, A.A., Kour, S., Cherry, J.D., Ramesh, N., Gleixner, A., Schwartz, J.C., Ebmeier, C., Old, W., Donnelly, C.J., et al. (2021). Traumatic injury compromises nucleocytoplasmic transport and leads to TDP-43 pathology. ELife *10*, e67587.

Arribere, J.A., Bell, R.T., Fu, B.X., Artiles, K.L., Hartman, P.S., and Fire, A.Z. (2014). Efficient marker-free recovery of custom genetic modifications with CRISPR/Cas9 in Caenorhabditis elegans. Genetics *198*, 837-846.

Bayliss, R., Ribbeck, K., Akin, D., Kent, H., Feldherr, C., Gorlich, D., and Stewart, M. (1999). Interaction Between NTF2 and xFxFG-containing Nucleoporins is Required to Mediate Nuclear Import of RanGDP. J. Mol. Biol. *293*, 579-593.

Beckhelling, C., Chang, P., Chevalier, S., Ford, C., and Houliston, E. (2003). Pre-M Phase-promoting Factor Associates with Annulate Lamellae in *Xenopus* Oocytes and Egg Extracts. Mol. Biol. Cell *14*, 1125–1137.

Brenner, S. (1974). The genetics of Caenorhabditis elegans. Genetics *77*, 71-94.

Chandra, S., and Lusk, C.P. (2022). Emerging Connections between Nuclear Pore Complex Homeostasis and ALS. Int. J. Mol. Sci. *23*, 1329.

Chandra, B., Michmerhuizen, N.L., Shirnekhi, H.K., Tripathi, S., Pioso, B.J., Baggett, D.W., Mitrea, D.M., Iacobucci, I., White, M.R., Chen, J., et al. (2022). Phase Separation Mediates NUP98 Fusion Oncoprotein Leukemic Transformation. Cancer Discov. *12*, 1152–1169.

Chase, D., Serafinas, C., Ashcroft, N., Kosinski, M., Longo, D., Ferris, D.K., and Golden, A. (2000). The polo-like kinase PLK-1 is required for nuclear envelope breakdown and the completion of meiosis in Caenorhabditis elegans. Genesis *26*, 26–41.

Cho, N.H., Cheveralls, K.C., Brunner, A.D., Kim, K., Michaelis, A.C., Raghavan, P., Kobayashi, H., Savy, L., Li, J.Y., Canaj, H., et al. (2022). OpenCell: Endogenous tagging for the cartography of human cellular organization. Science *375*, eabi6983.

Cohen-Fix, O., and Askjaer, P. (2017). Cell Biology of the *Caenorhabditis elegans* Nucleus. Genetics *205*, 25–59.

Colombi, P., Webster, B.M., Fröhlich, F., and Lusk, C.P. (2013). The transmission of nuclear pore complexes to daughter cells requires a cytoplasmic pool of Nsp1. J. Cell Biol. *203*, 215–232.

Cordes, V.C., Reidenbach, S., and Franke, W.W. (1996). Cytoplasmic annulate lamellae in cultured cells: composition, distribution, and mitotic behavior. Cell Tissue Res. *284*, 177–191.

D'Angelo, M.A., Raices, M., Panowski, S.H., and Hetzer, M.W. (2009). Age-Dependent Deterioration of Nuclear Pore Complexes Causes a Loss of Nuclear Integrity in Postmitotic Cells. Cell *136*, 284–295.

Davis, L.I., and Blobel, G. (1986). Identification and characterization of a nuclear pore complex protein. Cell *45*, 699–709.

De Souza, C.P.C., Osmani, A.H., Hashmi, S.B., and Osmani, S.A. (2004). Partial Nuclear Pore Complex Disassembly during Closed Mitosis in Aspergillus nidulans. Curr. Biol. *14*, 1973–1984.

Dimitriadi, M., and Hart, A.C. (2010). Neurodegenerative disorders: Insights from the nematode Caenorhabditis elegans. Neurobiol. Dis. *40*, 4–11.

Dokshin, G.A., Ghanta, K.S., Piscopo, K.M., and Mello, C.C. (2018). Robust Genome Editing with Short Single-Stranded and Long, Partially Single-Stranded DNA Donors in *Caenorhabditis elegans*. Genetics *210*, 781–787.

Elaswad, M.T., Munderloh, C., Watkins, B.M., Sharp, K.G., Breton, E., and Schisa, J.A. (2022). Imaging-associated stress causes divergent phase transitions of RNA-binding proteins in the *Caenorhabditis elegans* germ line. G3 GenesGenomesGenetics jkac172.

Fallini, C., Khalil, B., Smith, C.L., and Rossoll, W. (2020). Traffic jam at the nuclear pore: All roads lead to nucleocytoplasmic transport defects in ALS/FTD. Neurobiol. Dis. *140*, 104835.

Fan, X., De Henau, S., Feinstein, J., Miller, S.I., Han, B., Frøkjær-Jensen, C., and Griffin, E.E. (2020). SapTrap Assembly of *Caenorhabditis elegans* MosSCI Transgene Vectors. G3 GenesGenomesGenetics *10*, 635–644.

Fornerod, M., van Deursen, J., van Baal, S., Reynolds, A., Davis, D., Murti, K., Fransen, J., and Grosveld, G. (1997). The human homologue of yeast CRM1 is in a dynamic subcomplex with CAN/Nup214 and a novel nuclear pore component Nup88. EMBO J. *16*, 807–816.

Forsythe, M.E., Love, D.C., Lazarus, B.D., Kim, E.J., Prinz, W.A., Ashwell, G., Krause, M.W., and Hanover, J.A. (2006). *Caenorhabditis elegans* ortholog of a diabetes susceptibility locus: *oga-1* (*O*-GlcNAcase) knockout impacts *O* -GlcNAc cycling, metabolism, and dauer. Proc. Natl. Acad. Sci. *103*, 11952–11957.

Frey, S., and Görlich, D. (2007). A Saturated FG-Repeat Hydrogel Can Reproduce the Permeability Properties of Nuclear Pore Complexes. Cell *130*, 512–523.

Frey, S., Richter, R.P., and Görlich, D. (2006). FG-Rich Repeats of Nuclear Pore Proteins Form a Three-Dimensional Meshwork with Hydrogel-Like Properties. Science *314*, 815–817.

Galy, V., Mattaj, I.W., and Askjaer, P. (2003). Caenorhabditis elegans Nucleoporins Nup93 and Nup205 Determine the Limit of Nuclear Pore Complex Size Exclusion In Vivo. Mol. Biol. Cell *14*, 5104-5115.

Galy, V., Antonin, W., Jaedicke, A., Sachse, M., Santarella, R., Haselmann, U., and Mattaj, I. (2008). A role for gp210 in mitotic nuclear-envelope breakdown. J. Cell Sci. *121*, 317–328.

Gasset-Rosa, F., Lu, S., Yu, H., Chen, C., Melamed, Z., Guo, L., Shorter, J., Da Cruz, S., and Cleveland, D.W. (2019). Cytoplasmic TDP-43 De-mixing Independent of Stress Granules Drives Inhibition of Nuclear Import, Loss of Nuclear TDP-43, and Cell Death. Neuron *102*, 339-357.

Gleixner, A.M., Verdone, B.M., Otte, C.G., Anderson, E.N., Ramesh, N., Shapiro, O.R., Gale, J.R., Mauna, J.C., Mann, J.R., Copley, K.E., et al. (2022). NUP62 localizes to ALS/FTLD pathological assemblies and contributes to TDP-43 insolubility. Nat. Commun. *13*, 3380.

Gómez-Saldivar, G., Fernandez, A., Hirano, Y., Mauro, M., Lai, A., Ayuso, C., Haraguchi, T., Hiraoka, Y., Piano, F., and Askjaer, P. (2016). Identification of Conserved MEL-28/ELYS Domains with Essential Roles in Nuclear Assembly and Chromosome Segregation. PLOS Genet. *12*, e1006131.

Griffis, E.R., Xu, S., and Powers, M.A. (2003). Nup98 Localizes to Both Nuclear and Cytoplasmic Sides of the Nuclear Pore and Binds to Two Distinct Nucleoporin Subcomplexes. Mol. Biol. Cell *14*, 600–610.

Guo, L., Kim, H.J., Wang, H., Monaghan, J., Freyermuth, F., Sung, J.C., O’Donovan, K., Fare, C.M., Diaz, Z., Singh, N., et al. (2018). Nuclear-Import Receptors Reverse Aberrant Phase Transitions of RNA-Binding Proteins with Prion-like Domains. Cell *173*, 677-692.

Hamed, M., Caspar, B., Port, S.A., and Kehlenbach, R.H. (2021). A nuclear export sequence promotes CRM1-dependent targeting of the nucleoporin Nup214 to the nuclear pore complex. J. Cell Sci. *134*, jcs258095.

Hampoelz, B., Mackmull, M.T., Machado, P., Ronchi, P., Bui, K.H., Schieber, N., Santarella-Mellwig, R., Necakov, A., Andrés-Pons, A., Philippe, J.M., et al. (2016). Pre-assembled Nuclear Pores Insert into the Nuclear Envelope during Early Development. Cell *166*, 664–678.

Hampoelz, B., Andres-Pons, A., Kastritis, P., and Beck, M. (2019a). Structure and Assembly of the Nuclear Pore Complex. Annu. Rev. Biophys. *48*, 515–536.

Hampoelz, B., Schwarz, A., Ronchi, P., Bragulat-Teixidor, H., Tischer, C., Gaspar, I., Ephrussi, A., Schwab, Y., and Beck, M. (2019b). Nuclear Pores Assemble from Nucleoporin Condensates During Oogenesis. Cell *179*, 671-686.

Hanover, J.A., Forsythe, M.E., Hennessey, P.T., Brodigan, T.M., Love, D.C., Ashwell, G., and Krause, M. (2005). A *Caenorhabditis elegans* model of insulin resistance: Altered macronutrient storage and dauer formation in an OGT-1 knockout. Proc. Natl. Acad. Sci. *102*, 11266–11271.

Harel, A., Chan, R.C., Lachish-Zalait, A., Zimmerman, E., Elbaum, M., and Forbes, D.J. (2003). Importin Negatively Regulates Nuclear Membrane Fusion and Nuclear Pore Complex Assembly. Mol. Biol. Cell *14*, 4387-4396.

Hattersley, N., Cheerambathur, D., Moyle, M., Stefanutti, M., Richardson, A., Lee, K.Y., Dumont, J., Oegema, K., and Desai, A. (2016). A Nucleoporin Docks Protein Phosphatase 1 to Direct Meiotic Chromosome Segregation and Nuclear Assembly. Dev. Cell *38*, 463–477.

Hofweber, M., Hutten, S., Bourgeois, B., Spreitzer, E., Niedner-Boblenz, A., Schifferer, M., Ruepp, M.-D., Simons, M., Niessing, D., Madl, T., et al. (2018). Phase Separation of FUS Is Suppressed by Its Nuclear Import Receptor and Arginine Methylation. Cell *173*, 706-719.

Huelgas-Morales, G., and Greenstein, D. (2018). Control of oocyte meiotic maturation in C. elegans. Semin. Cell Dev. Biol. *84*, 90–99.

Huelgas-Morales, G., Sanders, M., Mekonnen, G., Tsukamoto, T., and Greenstein, D. (2020). Decreased mechanotransduction prevents nuclear collapse in a *Caenorhabditis elegans* laminopathy. Proc. Natl. Acad. Sci. *117*, 31301–31308.

Hülsmann, B.B., Labokha, A.A., and Görlich, D. (2012). The Permeability of Reconstituted Nuclear Pores Provides Direct Evidence for the Selective Phase Model. Cell *150*, 738–751.

Hutten, S., and Dormann, D. (2020). Nucleocytoplasmic transport defects in neurodegeneration — Cause or consequence? Semin. Cell Dev. Biol. *99*, 151–162.

Hutten, S., Usluer, S., Bourgeois, B., Simonetti, F., Odeh, H.M., Fare, C.M., Czuppa, M., Hruska-Plochan, M., Hofweber, M., Polymenidou, M., et al. (2020). Nuclear Import Receptors Directly Bind to Arginine-Rich Dipeptide Repeat Proteins and Suppress Their Pathological Interactions. Cell Rep. *33*, 108538.

Iovine, M.K., Watkins, J.L., and Wente, S.R. (1995). The GLFG Repetitive Region of the Nucleoporin Nupll6p Interacts with Kap95p, an Essential Yeast Nuclear Import Factor. J. Cell Biol. *131*, 1699-1713.

Joseph-Strauss, D., Gorjánácz, M., Santarella-Mellwig, R., Voronina, E., Audhya, A., and Cohen-Fix, O. (2012). Sm protein down-regulation leads to defects in nuclear pore complex disassembly and distribution in C. elegans embryos. Dev. Biol. *365*, 445–457.

Jud, M.C., Czerwinski, M.J., Wood, M.P., Young, R.A., Gallo, C.M., Bickel, J.S., Petty, E.L., Mason, J.M., Little, B.A., Padilla, P.A., et al. (2008). Large P body-like RNPs form in C. elegans oocytes in response to arrested ovulation, heat shock, osmotic stress, and anoxia and are regulated by the major sperm protein pathway. Dev. Biol. *318*, 38–51.

Kessel, G. (1989). Annulate lamellae - From obscurity to spotlight. Electron Micros Rev. *2*, 257-348.

Kutay, U., Jühlen, R., and Antonin, W. (2021). Mitotic disassembly and reassembly of nuclear pore complexes. Trends Cell Biol. *31*, 1019–1033.

Labokha, A.A., Gradmann, S., Frey, S., Hülsmann, B.B., Urlaub, H., Baldus, M., and Görlich, D. (2012). Systematic analysis of barrier-forming FG hydrogels from Xenopus nuclear pore complexes. EMBO J. *32*, 204–218.

Langerak, S., Trombley, A., Patterson, J.R., Leroux, D., Couch, A., Wood, M.P., and Schisa, J.A. (2019). Remodeling of the endoplasmic reticulum in Caenorhabditis elegans oocytes is regulated by CGH-1. Genesis *57*.

Lapierre, L.R. (2013). The TFEB orthologue HLH-30 regulates autophagy and modulates longevity in Caenorhabditis elegans. Nat. Commun. *4*, 2267.

Laurell, E., Beck, K., Krupina, K., Theerthagiri, G., Bodenmiller, B., Horvath, P., Aebersold, R., Antonin, W., and Kutay, U. (2011). Phosphorylation of Nup98 by Multiple Kinases Is Crucial for NPC Disassembly during Mitotic Entry. Cell *144*, 539–550.

Lee, B.E., Suh, P.-G., and Kim, J.I. (2021). O-GlcNAcylation in health and neurodegenerative diseases. Exp. Mol. Med. *53*, 1674–1682.

Linder, M.I., Köhler, M., Boersema, P., Weberruss, M., Wandke, C., Marino, J., Ashiono, C., Picotti, P., Antonin, W., and Kutay, U. (2017). Mitotic Disassembly of Nuclear Pore Complexes Involves CDK1- and PLK1-Mediated Phosphorylation of Key Interconnecting Nucleoporins. Dev. Cell *43*, 141-156.

Longtine, M.S., Mckenzie III, A., Demarini, D.J., Shah, N.G., Wach, A., Brachat, A., Philippsen, P., and Pringle, J.R. (1998). Additional modules for versatile and economical PCR-based gene deletion and modification in Saccharomyces cerevisiae. Yeast *14*, 953–961.

Makio, T., Stanton, L.H., Lin, C.C., Goldfarb, D.S., Weis, K., and Wozniak, R.W. (2009). The nucleoporins Nup170p and Nup157p are essential for nuclear pore complex assembly. J. Cell Biol. *185*, 459–473.

Mansfeld, J., Güttinger, S., Hawryluk-Gara, L.A., Panté, N., Mall, M., Galy, V., Haselmann, U., Mühlhäusser, P., Wozniak, R.W., Mattaj, I.W., et al. (2006). The Conserved Transmembrane Nucleoporin NDC1 Is Required for Nuclear Pore Complex Assembly in Vertebrate Cells. Mol. Cell *22*, 93–103.

Martino, L., Morchoisne-Bolhy, S., Cheerambathur, D.K., Van Hove, L., Dumont, J., Joly, N., Desai, A., Doye, V., and Pintard, L. (2017). Channel Nucleoporins Recruit PLK-1 to Nuclear Pore Complexes to Direct Nuclear Envelope Breakdown in C. elegans. Dev. Cell *43*, 157-171.

Mauro, M.S., Celma, G., Zimyanin, V., Magaj, M.M., Gibson, K.H., Redemann, S., and Bahmanyar, S. (2022). Ndc1 drives nuclear pore complex assembly independent of membrane biogenesis to promote nuclear formation and growth. ELife *11*, e75513.

Nachury, M.V., Maresca, T.J., Salmon, W.C., Waterman-Storer, C.M., Heald, R., and Weis, K. Importin Is a Mitotic Target of the Small GTPase Ran in Spindle Assembly. Cell *104*, 95-106.

Ng, S.C., Güttler, T., and Görlich, D. (2021). Recapitulation of selective nuclear import and export with a perfectly repeated 12mer GLFG peptide. Nat. Commun. *12*, 4047.

Onischenko, E., Tang, J.H., Andersen, K.R., Knockenhauer, K.E., Vallotton, P., Derrer, C.P., Kralt, A., Mugler, C.F., Chan, L.Y., Schwartz, T.U., et al. (2017). Natively Unfolded FG Repeats Stabilize the Structure of the Nuclear Pore Complex. Cell *171*, 904-917.

Onischenko, E.A., Gubanova, N.V., Kieselbach, T., Kiseleva, E.V., and Hallberg, E. (2004). Annulate Lamellae Play Only a Minor Role in the Storage of Excess Nucleoporins in Drosophila Embryos: Annulate Lamellae Assembly in Drosophila. Traffic *5*, 152–164.

Onischenko, E.A., Gubanova, N.V., Kiseleva, E.V., and Hallberg, E. (2005). Cdk1 and Okadaic Acid-sensitive Phosphatases Control Assembly of Nuclear Pore Complexes in Drosophila Embryos. Mol. Biol. Cell *16*, 5152-5162.

Padavannil, A., Sarkar, P., Kim, S.J., Cagatay, T., Jiou, J., Brautigam, C.A., Tomchick, D.R., Sali, A., D'Arcy, S., and Chook, Y.M. (2019). Importin-9 wraps around the H2A-H2B core to act as nuclear importer and histone chaperone. ELife *8*, e43630.

Paix, A., Folkmann, A., and Seydoux, G. (2017). Precision genome editing using CRISPR-Cas9 and linear repair templates in C. elegans. Methods *121–122*, 86–93.

Patel, S.S., Belmont, B.J., Sante, J.M., and Rexach, M.F. (2007). Natively Unfolded Nucleoporins Gate Protein Diffusion across the Nuclear Pore Complex. Cell *129*, 83–96.

Patterson, J.R., Wood, M.P., and Schisa, J.A. (2011). Assembly of RNP granules in stressed and aging oocytes requires nucleoporins and is coordinated with nuclear membrane blebbing. Dev. Biol. *353*, 173–185.

Pitt, J.N., Schisa, J.A., and Priess, J.R. (2000). P Granules in the Germ Cells of Caenorhabditis elegans Adults Are Associated with Clusters of Nuclear Pores and Contain RNA. Dev. Biol. *219*, 315–333.

Port, S.A., Monecke, T., Dickmanns, A., Spillner, C., Hofele, R., Urlaub, H., Ficner, R., and Kehlenbach, R.H. (2015). Structural and Functional Characterization of CRM1-Nup214 Interactions Reveals Multiple FG-Binding Sites Involved in Nuclear Export. Cell Rep. *13*, 690–702.

Raghunayakula, S., Subramonian, D., Dasso, M., Kumar, R., and Zhang, X.D. (2015). Molecular Characterization and Functional Analysis of Annulate Lamellae Pore Complexes in Nuclear Transport in Mammalian Cells. PLOS ONE *10*, e0144508.

Rahman, M.M., Munzig, M., Kaneshiro, K., Lee, B., Strome, S., Müller-Reichert, T., and Cohen-Fix, O. (2015). *Caenorhabditis elegans* polo-like kinase PLK-1 is required for merging parental genomes into a single nucleus. Mol. Biol. Cell *26*, 4718–4735.

Ren, H., Xin, G., Jia, M., Zhu, S., Lin, Q., Wang, X., Jiang, Q., and Zhang, C. (2019). Postmitotic annulate lamellae assembly contributes to nuclear envelope reconstitution in daughter cells. J. Biol. Chem. *294*, 10383–10391.

Ribbeck, K., and Görlich, D. (2001). Kinetic analysis of translocation through nuclear pore complexes. EMBO J. *20*, 1320–1330.

Ritterhoff, T., Das, H., Hofhaus, G., Schröder, R.R., Flotho, A., and Melchior, F. (2016). The RanBP2/RanGAP1*SUMO1/Ubc9 SUMO E3 ligase is a disassembly machine for Crm1-dependent nuclear export complexes. Nat. Commun. *7*, 11482.

Robinson, J.S., Klionsky, D.J., Banta, L.M., and Emr, S.D. (1988). Protein sorting in Saccharomyces cerevisiae: isolation of mutants defective in the delivery and processing of multiple vacuolar hydrolases. Mol Cell Biol. *8*, 4936-4948.

Ródenas, E., Klerkx, E.P., Ayuso, C., Audhya, A., and Askjaer, P. (2009). Early embryonic requirement for nucleoporin Nup35/NPP-19 in nuclear assembly. Dev. Biol. *327*, 399–409.

Ródenas, E., González-Aguilera, C., Ayuso, C., and Askjaer, P. (2012). Dissection of the NUP107 nuclear pore subcomplex reveals a novel interaction with spindle assembly checkpoint protein MAD1 in *Caenorhabditis elegans*. Mol. Biol. Cell *23*, 930–944.

Ruba, A., and Yang, W. (2016). O-GlcNAcylation in the Nuclear Pore Complex. Cell. Mol. Bioeng. *9*, 227–233.

Schedl, T., and Kimble, J. (1988). fog-2, a germ-line-specific sex determination gene required for hermaphrodite spermatogenesis in Caenorhabditis elegans. Genetics *119*, 43–61.

Schmidt, H.B., and Görlich, D. (2015). Nup98 FG domains from diverse species spontaneously phase-separate into particles with nuclear pore-like permselectivity. ELife *4*, e04251.

Schmidt, H.B., and Görlich, D. (2016). Transport Selectivity of Nuclear Pores, Phase Separation, and Membraneless Organelles. Trends Biochem. Sci. *41*, 46–61.

Schwartz, M.L., and Jorgensen, E.M. (2016). SapTrap, a Toolkit for High-Throughput CRISPR/Cas9 Gene Modification in *Caenorhabditis elegans*. Genetics *202*, 1277–1288.

Sheth, U., Pitt, J., Dennis, S., and Priess, J.R. (2010). Perinuclear P granules are the principal sites of mRNA export in adult *C. elegans* germ cells. Development *137*, 1305–1314.

Shirayama, M., Seth, M., Lee, H.C., Gu, W., Ishidate, T., Conte, D., and Mello, C.C. (2012). piRNAs Initiate an Epigenetic Memory of Nonself RNA in the C. elegans Germline. Cell *150*, 65–77.

Silvestrini, M.J., Johnson, J.R., Kumar, A.V., Thakurta, T.G., Blais, K., Neill, Z.A., Marion, S.W., St. Amand, V., Reenan, R.A., and Lapierre, L.R. (2018). Nuclear Export Inhibition Enhances HLH-30/TFEB Activity, Autophagy, and Lifespan. Cell Rep. *23*, 1915–1921.

Springhower, C.E., Rosen, M.K., and Chook, Y.M. (2020). Karyopherins and condensates. Curr. Opin. Cell Biol. *64*, 112–123.

Stafstrom, J.P., and Staehelin, L.A. (1984). Are annulate lamellae in the Drosophila embryo the result of overproduction of nuclear pore components? J. Cell Biol. *98*, 699–708.

Strawn, L.A., Shen, T., Shulga, N., Goldfarb, D.S., and Wente, S.R. (2004). Minimal nuclear pore complexes define FG repeat domains essential for transport. Nat. Cell Biol. *6*, 197–206.

Sun, H., and Hobert, O. (2021). Temporal transitions in the post-mitotic nervous system of Caenorhabditis elegans. Nature *600*, 93–99.

Sun, Q., Carrasco, Y.P., Hu, Y., Guo, X., Mirzaei, H., MacMillan, J., and Chook, Y.M. (2013). Nuclear export inhibition through covalent conjugation and hydrolysis of Leptomycin B by CRM1. Proc. Natl. Acad. Sci. *110*, 1303–1308.

Tan, P.S., Aramburu, I.V., Mercadante, D., Tyagi, S., Chowdhury, A., Spitz, D., Shammas, S.L., Gräter, F., and Lemke, E.A. (2018). Two Differential Binding Mechanisms of FG-Nucleoporins and Nuclear Transport Receptors. Cell Rep. *22*, 3660–3671.

Terlecki-Zaniewicz, S., Humer, T., Eder, T., Schmoellerl, J., Heyes, E., Manhart, G., Kuchynka, N., Parapatics, K., Liberante, F.G., Müller, A.C., et al. (2021). Biomolecular condensation of NUP98 fusion proteins drives leukemogenic gene expression. Nat. Struct. Mol. Biol. *28*, 190–201.

The C. elegans Deletion Mutant Consortium (2012). Large-Scale Screening for Targeted Knockouts in the Caenorhabditis elegans Genome. G3 GenesGenomesGenetics *2*, 1415-1425.

Thomas, L.L., van der Vegt, S.A., and Fromme, J.C. (2019). A Steric Gating Mechanism Dictates the Substrate Specificity of a Rab-GEF. Dev. Cell *48*, 100-114.

Timmons, L., and Fire, A. (1998). Specific interference by ingested dsRNA. Nature *395*, 854–854.

Toyama, B.H., Savas, J.N., Park, S.K., Harris, M.S., Ingolia, N.T., Yates, J.R., and Hetzer, M.W. (2013). Identification of Long-Lived Proteins Reveals Exceptional Stability of Essential Cellular Structures. Cell *154*, 971–982.

Urso, S.J., Comly, M., Hanover, J.A., and Lamitina, T. (2020). The O-GlcNAc transferase OGT is a conserved and essential regulator of the cellular and organismal response to hypertonic stress. PLOS Genet. *16*, e1008821.

Vicencio, J., Martinez-Fernandez, C., Serrat, X., and Ceron, J. (2019). Efficient generation of endogenous fluorescent reporters by nested CRISPR in Caenorhabditis elegans. Genetics *211*, 1143-1154.

Walther, T.C., Askjaer, P., Gentzel, M., Habermann, A., Griffiths, G., Wilm, M., Mattaj, I.W., and Hetzer, M. (2003). RanGTP mediates nuclear pore complex assembly. Nature *424*, 689–694.

Wippich, F., Bodenmiller, B., Trajkovska, M.G., Wanka, S., Aebersold, R., and Pelkmans, L. (2013). Dual Specificity Kinase DYRK3 Couples Stress Granule Condensation/Dissolution to mTORC1 Signaling. Cell *152*, 791–805.

Wu, X., Kasper, L.H., Mantcheva, R.T., Mantchev, G.T., Springett, M.J., and van Deursen, J.M.A. (2001). Disruption of the FG nucleoporin NUP98 causes selective changes in nuclear pore complex stoichiometry and function. Proc. Natl. Acad. Sci. *98*, 3191–3196.

Xu, S., and Powers, M.A. (2013). In vivo analysis of human nucleoporin repeat domain interactions. Mol. Biol. Cell *24*, 1222–1231.

Xylourgidis, N., Roth, P., Sabri, N., Tsarouhas, V., and Samakovlis, C. (2006). The nucleoporin Nup214 sequesters CRM1 at the nuclear rim and modulates NFκB activation in *Drosophila*. J. Cell Sci. *119*, 4409–4419.

Yoo, T.Y., and Mitchison, T.J. (2021). *O*-GlcNAc modification of nuclear pore complexes accelerates bidirectional transport. J. Cell Biol. *220*, e202010141.

Yoshida, K., Seo, H.S., Debler, E.W., Blobel, G., and Hoelz, A. (2011). Structural and functional analysis of an essential nucleoporin heterotrimer on the cytoplasmic face of the nuclear pore complex. Proc. Natl. Acad. Sci. *108*, 16571–16576.

Zhang, K., Daigle, J.G., Cunningham, K.M., Coyne, A.N., Ruan, K., Grima, J.C., Bowen, K.E., Wadhwa, H., Yang, P., Rigo, F., et al. (2018). Stress Granule Assembly Disrupts Nucleocytoplasmic Transport. Cell *173*, 958-971.

Zheleva, A., Gómez-Orte, E., Sáenz-Narciso, B., Ezcurra, B., Kassahun, H., de Toro, M., Miranda-Vizuete, A., Schnabel, R., Nilsen, H., and Cabello, J. (2019). Reduction of mRNA export unmasks different tissue sensitivities to low mRNA levels during Caenorhabditis elegans development. PLOS Genet. *15*, e1008338.

Zhou, M.H., and Yang, Q.M. (2014). NUP214 fusion genes in acute leukemia. Oncol. Lett. *8*, 959–962.